

# NON-LINEAR PHENOMENA IN GRANULAR MATERIALS

BY THEODORE LORDIN SIU

A dissertation submitted to the  
Graduate School—New Brunswick  
Rutgers, The State University of New Jersey  
in partial fulfillment of the requirements  
for the degree of  
Doctor of Philosophy  
Graduate Program in Physics and Astronomy

Written under the direction of  
Troy Shinbrot  
and approved by

---

---

---

---

New Brunswick, New Jersey

October, 2016

## ABSTRACT OF THE DISSERTATION

### Non-linear Phenomena in Granular Materials

by Theodore Lordin Siu

Dissertation Director: Troy Shinbrot

Granular materials are quite common in our everyday lives in both nature and industry. Yet much of the phenomena that they exhibit is not well understood and in fact quite complex and non-linear. For example, it has been known since Faraday's time that swirling sandstorms are able to generate electric charge that manifest as multi-million volt lightning discharges. Poured glass beads have been demonstrated to also charge electrically, causing random ejections of grains and creating interesting raised clump structures known as razorbacks. Lastly, granular materials are known to exhibit self-segregation based on size. An example of this phenomenon is the landscape observed on the asteroid 25143/Itokawa, which has spatially separated boulder fields and sand seas.

In this work, we discuss three projects that examine non-linear behavior in granular materials. In our first chapter, we discuss a computational electrostatic model of vibrated identical granular particles. We show in our model that granular materials are able to exponentially generate charge and polarization through  $1/r^2$  electric field interactions. By adding neutralization between neighboring particles, we find complex phenomena such as charge and polarization waves that propagate through the particles. In closing, we reproduce a polarized state experimentally using vibrated glass beads which represents one of the phenomena that we observe in our model phase diagram;

we also discuss our experimental efforts to image charge and polarization waves.

In the second chapter, we examine the dynamical behavior of charged granular particles. We find that by experimentally exposing grains to simple electric fields, a number of novel behaviors appear including dust clouds, dust columns and tendrils. In addition, in our experiments and simulations we find evidence for non-linear electrostatic interactions between particles including asymmetries and particle trajectories that do not adhere to naive electric field lines.

In our final chapter, we deal with granular segregation found on the asteroid known as 25143/Itokawa. On the asteroid there exists segregation between smaller sized dust and rocks on the centimeter size, from large boulders with diameters on the order of meters. While current explanations attribute the segregation to the phenomenon known as the Brazil Nut Effect, we show that “ballistic segregation” or a difference of collision types on the asteroid surface can be responsible for the separation between different sized particles. We show that the surface area growth of particles can be modeled using the non-linear Hill Equation, which shows that increasing amounts of dust accumulation promotes further dust accumulation.

## Acknowledgements

First and foremost I would like to thank my advisor Troy Shinbrot for giving a physics graduate student a chance to study granular materials and soft condensed matter. Troy is the consummate researcher; he is incredibly smart with a deep knowledge of math, physics, engineering and biology, he is inquisitive, and he is eloquent in both speech and writing. In addition Troy is patient, encouraging, and kind. I would like to thank him for always being invested in our projects, for always taking the time out to answer my questions and discuss technical details of our work, for encouraging me to pursue the topics that interested me the most, and for always believing in me and my work even when I was not always confident. Credit also goes to my many colleagues including Nam Kim, Jake Cotton, Greg Mattson, Miguel Vivar, Junren Wang from Kent State and Kate O'Neill. It was a pleasure working with you all. Thank you for discussing science with me and providing me with many ideas that I would not be able to come up on my own.

Next I would like to thank my wife Esther. Your love has always lifted me up. Thank you for always caring for me with your words and actions. We have many adventures left to go on! A huge thank you also to my family, Mom, Baba, Elliot, Lauryn, and Darren, for their love and support through this whole graduate school journey. Thank you for your unconditional love, the nice warm meals after a long day of work, the encouraging phone calls and the many laughs and jokes. Also a special thank you goes out to Darren who came by to assist on one of my experiments late at night during my first year of research.

Another huge thank you goes to my many friends that I have met at graduate school- Wenbo Wang, Juho Lee, Bismayan Chakrabarti, Pasha Khromov and Dima Galakhov. Thank you for staying up with me to do homework, discussing physics problems with me

and being great friends. To my friends at CLG, BLG and PCC thank you for keeping me grounded and reminding me that there is purpose outside of graduate school.

I would like to thank my many mentors in physics over the years. My first physics class was in high school taught by Diane Minsavage. She was supportive and helpful. Her classes gave me confidence that physics was not as difficult as everyone made it out to be. In 2010, I did a research stint with Stephanie Wissel at PPPL and student taught with Christine Osborne. Both of them encouraged me to apply to physics graduate school. I would like to thank them for being the final pushes for undertaking this Ph.D. It has been rough at times but I have grown a lot through this experience not only as a physicist but also as a person.

Finally, I would like to thank God for putting me on this journey and allowing me to learn more about this beautiful, complex world. We currently live in a fractured time where many people do not think science and religion can co-exist. I hope that this will change in the future. Soli Deo Gloria.

## Publications and preprints associated with this dissertation

1. Sebastian Bianchini, Alejandro Lage, **Theo Siu**, Troy Shinbrot, Ernesto Altshuler (2013) Upstream Contamination of Floating Particles *Proceedings of the Royal Society A*
2. **Theo Siu**, Jake Cotton, Gregory Mattson, Troy Shinbrot. (2014) Self Sustaining Charging Of Identical Particles *Physical Review E* 89
3. **Theo Siu**, Will Pittman, Jake Cotton, Troy Shinbrot. (2015) Non-linear Granular Electrostatics *Granular Matter* 17
4. Troy Shinbrot, Tapan Sabuwala , **Theo Siu**, Miguel Vivar Lazo, Pinaki Chakraborty. Size segregation in the rubble-pile asteroid Itokawa (*Pre-Print*)

Materials from this dissertation have been publicly presented at the following conferences:

1. APS March Meeting, 2014, Denver, CO
2. Granular and Granular Fluid Flow Gordon Conference, 2014, Stonehill College, Easton, MA
3. APS March Meeting, 2015, San Antonio, TX
4. APS March Meeting 2016, Baltimore, MD

## Dedication

Dedicated to my parents.

# Table of Contents

<b>Abstract</b> . . . . .	ii
<b>Acknowledgements</b> . . . . .	iv
<b>Dedication</b> . . . . .	vii
<b>List of Figures</b> . . . . .	x
<b>1. Introduction</b> . . . . .	1
1.0.1. Large Scale Electrical Charging in Granular Systems . . . . .	1
1.0.2. Complex Trajectories from Multibody $\frac{1}{r^2}$ fields . . . . .	4
1.0.3. Granular Segregation . . . . .	5
<b>2. Self Sustaining Charging Between Identical Colliding Particles</b> . . .	6
2.1. Introduction . . . . .	6
2.2. 1D Dipole Lattice Simulation . . . . .	7
2.2.1. Polarization . . . . .	7
2.2.2. Neutralization . . . . .	8
2.2.3. Boundary conditions . . . . .	9
2.2.4. Simulation Results . . . . .	9
2.2.5. Experimental Confirmation . . . . .	17
Vibrated Bed of Beads . . . . .	17
Charge Imaging with Polymer Disperse Liquid Crystals . . . . .	20
2.2.6. Concluding remarks . . . . .	22
<b>3. Non-Linear Dynamics</b> . . . . .	25
3.1. Introduction . . . . .	25
3.2. Experiments . . . . .	28



3.2.1. Experimental Phase Diagram . . . . .	30
3.3. Simulations . . . . .	32
3.3.1. Computational Phase Diagram . . . . .	39
3.4. Discussion . . . . .	42
3.4.1. Non-uniqueness . . . . .	42
3.4.2. Outlook . . . . .	44
<b>4. Size segregation in the rubble-pile asteroid Itokawa . . . . .</b>	<b>45</b>
<b>5. Conclusion . . . . .</b>	<b>57</b>
<b>Bibliography . . . . .</b>	<b>60</b>
<b>Appendix A. Polymer Disperse Liquid Crystal (PDLC) . . . . .</b>	<b>66</b>
A.1. PDLC Fabrication Methods . . . . .	66
A.1.1. Solvent Induced Phase Separation PDLC . . . . .	66
Polymer Induced Phase Separation PDLC . . . . .	66
Charge Imaging . . . . .	67
<b>Appendix B. Chapter 3 Supplementary Videos . . . . .</b>	<b>68</b>
<b>Appendix C. Chapter 4 Supplementary Materials . . . . .</b>	<b>69</b>
C.1. Supplementary Videos . . . . .	69
C.2. Uniformity of Bead Deposition . . . . .	70
C.3. Computational Boulder Shape . . . . .	73
<b>Appendix D. Upstream Contamination by Floating Particles . . . . .</b>	<b>74</b>
D.1. Upstream Contamination . . . . .	74
D.2. Supplementary Videos . . . . .	87
D.3. Tea Leaves flowing upstream into pot of initially clear water . . . . .	88
D.4. Clear water being pipetted into reservoir of water containing fluorescent particles. . . . .	89
D.5. Computational Simulations . . . . .	91

## List of Figures

1.1. Electrical charging mechanism in the presence of an external field. . . .	4
2.1. 1-D Dipole Lattice Simulation Results. . . . .	10
2.2. 1-D Lattice Phase Diagram. . . . .	12
2.3. Traveling Charge and Polarization Waves. . . . .	16
2.4. Vibrated Glass Beads Graph. . . . .	19
2.5. Opacity Changes in PDLC. . . . .	21
2.6. Alligator Clip Experiment. . . . .	22
3.1. A simple two particle example of non-linearity. . . . .	26
3.2. Experimental setup and results. . . . .	29
3.3. Experimental phase diagram. . . . .	31
3.4. Experimental Setup vs Simulation. . . . .	33
3.5. Simulation Trajectories 1. . . . .	37
3.6. Simulation Trajectories 2. . . . .	39
3.7. Computational Phase Diagram. . . . .	40
3.8. Experimental Phenomena. . . . .	42
4.1. Segregation of large and small grains. . . . .	48
4.2. Evaluation of cooperativity in deposition of small grains. . . . .	50
4.3. Discrete element simulations using LIGGGHTS of 1 mm diameter pebbles and larger stones dropped from fixed height but random horizontal positions onto fixed substrate. . . . .	56
C.1. Bead Deposition Graphs. . . . .	71
C.2. Shape of computational boulders. . . . .	73
D.1. Upstream Contamination Experiment . . . . .	75
D.2. Proposed mechanism for upstream contamination. . . . .	78

D.3. Upstream contamination in 4.5m long, 30cm wide, flume. . . . .	84
D.4. Upstream contamination of Mate Tea. . . . .	88
D.5. Upstream Contamination in pippetted water . . . . .	90

# Chapter 1

## Introduction

Granular materials are known to exhibit phenomena that are non-linear and complex [1–6]. Understanding non-linear granular phenomena may have many important applications including spark and explosion hazard detection [7,8], volcano eruption prediction [9–11], and more efficient and effective equipment for space travel [12,13]. This dissertation presents three projects that utilize table top experiments and computational simulations to examine three different types of non-linear behavior in granular materials: non-linear electrical polarization growth in granular materials, non-linear dynamical behavior of granular particles that results from applying strong external electric fields, and finally a model that we dub “ballistic segregation”, a collision model that may explain particle size segregation of rocks and dust as is observed on the asteroid 25143/Itokawa. An additional project on the upstream contamination of granular materials is included in the appendix.

In this first chapter, I give an introduction to key theories and models that my research builds upon: electrical charging due to particle size differences, electrical charging due to the presence of an external electric field, the non-linear three body gravitational model and existing models of granular segregation such as the Brazil Nut Effect [14] and the Reverse Brazil Nut Effect [15].

### 1.0.1 Large Scale Electrical Charging in Granular Systems

Dating back to Michael Faraday in 1850 [16], who mentioned the phenomenon of sandstorm lightning, researchers have long been interested in electrical charging in particle clouds. In addition to electrical charging in nature as seen in sandstorms [16,17], volcanic ash [9–11], and dust plumes [8], dust charges in industry have been known to

create sparks leading to dust explosions [7]. Finally, electrified dust in space has been reported to cling to spacesuits, jamming up joints and limiting the duration of space walks [12, 13]. Although there have been a number of proposed mechanisms that attribute the electrification of chemically identical particles to non-uniform heating, or differences in contact areas, we discuss two alternative theories that relate directly to our exponential polarization model that we present in Chapter 2.

Two hypotheses for the cause of electrification of granular materials are the following:

1. Lacks et al. [18–20] have attributed granular electrification to size differences between colliding grains. Previous works by Shaw [21] as well as Lowell and Truscott [22, 23] have shown that when rubbing together two chemically identical insulators, one with a smaller surface area on a larger surface area, the smaller surface area appears to gain a negative charge. Lowell and Truscott [22, 23] have argued that electrons trapped in high energy states are responsible for charge transfer between similar materials. When brought in contact with lower energy states on adjacent particles during collisions, high energy state electrons can quantum mechanically tunnel to those lower states. In Lack et al.’s work, the authors used simple geometric arguments in combination with electron tunneling to create a simple collisional model of charge transfer. They found that in the case of collisions with particles of unequal size, the smaller particles tended to charge negatively while the larger particle charged positively. As a result, with repeated random collisions, smaller sized particles should tend to charge more negatively than their larger counterparts. Lacks et al. extended their derivations to multiple collisions to come up with an expression for the net charge of a particle of a given size as a function of time.

On a related note, recent thermoluminescence measurements on insulated grains by Waitukaitis et al. [24] has shown that there are not enough high energy state electrons to account for the scale of charge transferred in granular materials. In their work, Waitukaitis and his colleagues performed two separate experiments.

Their first experiment involved dropping electrically charged grains, allowing the particles to fall freely via gravity, between two large copper plates held at a fixed potential difference. Using high precision cameras, they measured the particles' horizontal acceleration due to the electric field and were able to estimate the charge and surface density  $\sigma$  of trapped electrons on the grains before electrification. In the second experiment, they measured the photon emission rate of a heated sample of grains using a photomultiplier tube. They calculated a resulting charge density of trapped electrons in their sample that was 5 orders of magnitude less than was observed in their free fall experiments.

2. Shinbrot et al. [25] have shown that with particles of a single size, given an external electric field, granular materials can generate charge through polarization. In considering two colliding particles exposed to an electric field, one would expect that initially before any collision the two particles would polarize due to the electric field. Upon collision, the particles may neutralize, yet when they separate again, they repolarize leaving one of the particles to be net positive and the other particle net negative. This phenomenon is illustrated in Fig 1.1.

The authors supported their model by performing simulations of initially neutral, spherical particles that collided with one another under gravitation forces in a vibrated bed. Utilizing a polarization, neutralization, and subsequent repolarization mechanism, they found that particles exhibited an asymptotic mean net charge per particle after  $\sim 10^6$  time steps. Additionally, the depth of the particle bed appeared to affect the magnitude of mean charge. They compared their simulations to an actual experiment of a spouted bed-glass beads fluidized by air blown below. In the experiment, the container holding the glass beads was grounded on the bottom using a metal plate. On the top was another metal plate connected to a 30 kV Van De Graaf generator. They measured the number of levitated grains as a function of depth of granular bed and compared it with a similar plot in their simulations. They found strong agreement between experiment and simulation.

In our work, we present an alternative computational model where neither size

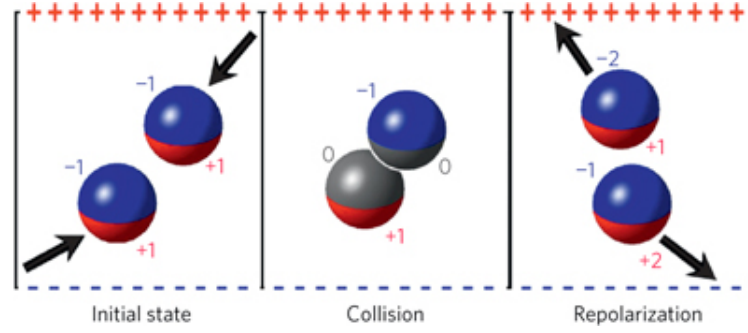


Figure 1.1: Electrical charging mechanism in the presence of an external field. In the presence of an electric field, two insulating particles will initially polarize. The numbers represent the charges of each of the particles' hemispheres. Upon collision, the touching hemispheres neutralize. When the particles separate and repolarize, they end up with non-zero net charges. Picture credit to [25]

difference nor the presence of an external electric field is necessary to produce a large magnitude of charge and polarization. We show that with identically sized particles in a 1-d lattice, a small perturbation of net polarization typically grows exponentially. When neutralization is introduced, we find the presence of travelling polarization and charge waves. In our experiments, we reproduce a polarized state that agrees with our simulations.

### 1.0.2 Complex Trajectories from Multibody $\frac{1}{r^2}$ fields

The three-body gravitational field problem has been studied for many years. Poincaré [26] was the first to show that although deterministic, the solution of the three body problem was not integrable and could not be expressed as function of the bodies' positions or velocities. In our simulations and experiments we study the behavior of grains subjected to electrical fields proportional to  $1/r^2$ . The particles polarize under the electric fields, exert forces on one another and subject further electric fields on one another causing repolarization. In our work, we find evidence of non-linear dynamical behavior along with a myriad of different phenomena including asymmetries, dust clouds and the formation of granular tendrils and columns.

### 1.0.3 Granular Segregation

Granular materials are known to exhibit segregation based on size. This segregation has typically been attributed to what is known as the Brazil Nut Effect [14]. In a vibrated bed of polydisperse particles with vertical walls, the larger, more massive particles tend to end up on the top. This effect has been subject to a number of parameters such as vibration frequency, friction, air flow, and particle density. Additionally, it has been attributed to several explanations including smaller particles more easily slipping underneath the larger ones (termed as “percolation”), and larger particles convecting up the center of the bed and getting trapped at the top- unable to fit into the narrow downward flows. A Reverse Brazil Nut Effect [15] has also been discovered where light large objects instead sink to the bottom of the bed.

While the Brazil Nut Effect has been known to explain granular segregation in closed environments, it has also been used to explain segregation on the asteroid 25413/Itokawa [27]. However, we argue that the asteroid surface does not have any vertical walls, has low gravity that is anisotropic and lacks periodic shaking. We offer a new model for granular segregation that is due to differences in collisional dissipation. We term the phenomenon “ballistic segregation”. We show that dust collisions with larger sized rocks and boulders cause the dust to bounce away. However dust collisions with other dust particles promotes further dust accumulation. Thus we end up with boulders segregated from sand seas.



## Chapter 2

# Self Sustaining Charging Between Identical Colliding Particles

### 2.1 Introduction

It has been known, at least since Faraday's time [16], that grains in desert sandstorms spontaneously generate multimillion volt electrical discharges. This effect has been attributed to differences in particle size or material [20]: Certainly a plausible explanation. At the same time, however, work spanning several decades in different laboratories and using different experimental systems has shown that even identical samples of a material [11, 19, 22, 23, 28, 29]-including particles of the same size, shape, and composition [25] - can spontaneously break symmetry and transfer charge from one to another. Moreover, once a charge has moved from one sample to another, further contacts will transport additional charges of the same sign in the same direction, against Coulomb forces, to produce monotonically increasing charges and fields [28, 29].

In the present chapter, we probe these findings through the examination of a simplified one-dimensional (1D) lattice of identical dielectric particles. We find that non-linear feedback between a particle and its neighbors can cause a single infinitesimally small dipole to grow exponentially rapidly in time. We confirm experimentally that identical colliding particles do generate a self-sustaining dipole field. Additionally, if adjacent particles in the lattice model are allowed to partially neutralize one another as they might through collisional interactions, we find that new states appear in which domains of like-polarization travel through the lattice. These results provide a mechanism by which collisional flows of identical grains can generate electric fields that grow and travel in complex ways.

## 2.2 1D Dipole Lattice Simulation

We begin by considering a 1D lattice of 1000 identical particles of unit diameter, spaced a fixed distance, also one unit, apart. The dynamics of this model consists of three essential elements prescribing first, the polarization of each particle due to its neighbors, second, partial neutralization of each adjacent particle pair meant to mimic effects of collision, and third, boundary conditions applied to the top and bottom particles. We define each element of the model here.

### 2.2.1 Polarization

Each particle  $i$  can host charges  $Q_i^{top}$  and  $Q_i^{bottom}$  at a vertical distance 0.375 from its center: In this manner, each particle can sustain a dipole moment  $P_i = \frac{3}{4}(Q_i^{top} - Q_i^{bottom})$ . Each particle feels an electric field  $E_i$  at its center due to the top and bottom charges of all of its neighbors. We calculate  $E_i$  directly using Coulomb's law, i.e.,  $E_i = \sum_{j \neq i} Q_j / r_{ij}^2$ , where  $r_{ij}$  is the distance from the center of the  $i$ th particle to the top and bottom charges on each of the other  $j$  particles. We assume that all particles are dielectric with the same susceptibility  $\chi_e$ , so that the  $i$ th particle will attain an induced dipole moment  $\chi_e \cdot E_i$ . This moment is added to whatever preexisting dipole may be present so that

$$P_i \rightarrow \frac{3}{4}(Q_i^{top} - Q_i^{bottom}) + \chi_e \cdot E_i \quad (2.1)$$

Explicitly, Eq. (2.1) combined with charge conservation implies that the top and bottom charges become

$$Q_i^{bottom} \rightarrow Q_i^{bottom} - \frac{2}{3}\chi_e \cdot E_i \quad (2.2)$$

$$Q_i^{top} \rightarrow Q_i^{top} + \frac{2}{3}\chi_e \cdot E_i \quad (2.3)$$

Thus, the polarization of a particle consists of two parts: A permanent ferroelectric polarization defined by its state following a collision and a transient paraelectric polarization slaved to the external field. We emphasize that except at the boundaries (which we discuss shortly), charge is conserved under all circumstances, however energy is not. That is, increasing polarization involves no gain or loss in net charge, however it does

require an input of energy. Thus we imagine that the lattice represents an agitated bed of grains in which the energy required to polarize molecules in one grain is provided by the mechanical energy needed to draw another polarized grain closer. In this way, periodic mechanical input of energy causes grains to repeatedly approach one another, generating an increase in polarization every time step. In a previous paper, we demonstrated that identical particles can develop large charges in this way after repeated contacts in the presence of a constant external electric field [8]. In the present calculations, we use precisely the same scheme without applying any external field. Since the field is provided by feedback between nearby particles according to Eq. (2.1), in principle a particles polarization could either increase or decrease, and indeed we will see from our simulations that both can occur.

We remark that the feedback of Eq. (2.1) implies an ordering to events: If particle A imparts a polarization on particle B and then particle B interacts with a third particle C, then the B-C interaction will produce a different result than if the A-B interaction had occurred later. This can be dealt with either by calculating all induced polarizations and then adding polarizations to the preexisting values at the end of each time step or by randomizing the order of interactions to eliminate systematic bias. We will compare calculations with a vibrated bed of nearly randomly [30] colliding particles, so we adopt the second alternative here.

### 2.2.2 Neutralization

To mimic a collisional granular flow, once per time step we allow each pair of adjacent particles, chosen in randomized order, to collide once. During each collision, we permit charges to partially neutralize with efficiency  $\eta$ . Explicitly,

$$Q_{i+1}^{bottom} \rightarrow (1 - \frac{\eta}{2})Q_{i+1}^{bottom} + \frac{\eta}{2}Q_i^{top} \quad (2.4)$$

$$Q_i^{top} \rightarrow (1 - \frac{\eta}{2})Q_i^{top} + \frac{\eta}{2}Q_{i+1}^{bottom} \quad (2.5)$$

so for  $\eta = 0$ , charges  $Q_i^{top}$  and  $Q_i^{bottom}$  remain unchanged after a simulated collision, and for  $\eta = 100\%$ , both charges revert to their average.

### 2.2.3 Boundary conditions

To close the description, we consider collisions on a grounded surface with a free upper boundary-as occurs, for example, in sandstorms or industrial dust clouds. So we ground the bottom of the bottom-most charge:  $Q_1^{bottom} \equiv 0$ , whereas the top of the topmost particle is treated like every other charge, except that it never encounters a neighbor above. As we have mentioned, charges are conserved in all collisions, except at the bottom boundary where a charge is added or removed to maintain the boundary condition  $Q_1^{bottom} \equiv 0$ . A final embellishment to the model is that we include image charges in the simplest possible way [31], as if the bottom surface were a perfect conductor. Simulations without image charges also were performed and do not differ noticeably from what we present here.

We make a technical clarification and then present results. Because we are ultimately interested in practical applications, we constrain the polarization to always lie within a maximum range, so  $|Pi| \leq P_{max}$ . This is realistic insofar as any real particle can sustain only a finite maximum charge separation beyond which dielectric breakdown will occur, but we will see momentarily that this is also computationally necessary to prevent polarizations from diverging. We choose  $P_{max} = 10$ , although other values have been found to produce nearly identical results.

### 2.2.4 Simulation Results

As a first test of this model, we consider the simplest case without neutralization, so  $\eta = 0$ , and we start with all but one of 1000 particles in the zero charge and polarization state,  $Q_i^{top} = Q_i^{bottom} = 0$ . We initialize the center particle with a tiny polarization  $P_{500} = 1.5 \times 10^{-9}$ , so  $Q_i^{top} = -Q_i^{bottom} = 10^{-9}$ . As shown in Fig. 2.1(a), the central particle's polarization grows along the solid curved line until it reaches  $P_{max}$ . That particle also recruits the polarizations of its neighbors, which similarly rapidly reach  $P_{max}$ . As shown in the semilogarithmic plot of Fig. 2.1(b), the cumulative sum of the particles' polarizations grows exponentially with two regimes: First a steep growth as the central particle's polarization escalates and then a more moderate, but still

exponential, growth as further particle polarizations are recruited. Reasonably enough, as the susceptibility increases, so does the rate at which polarization grows: This is shown in Fig. 2.1(d).

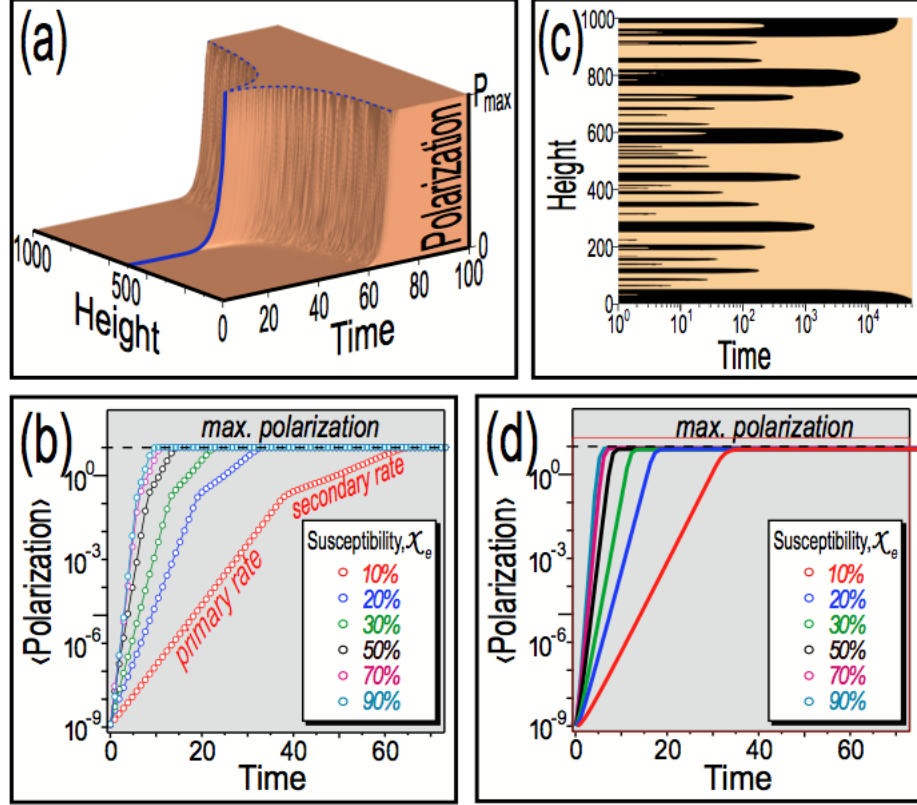


Figure 2.1: 1-D Dipole Lattice Simulation Results.

(a) Time evolution of polarizations of 1000 dielectric particles in a 1D array. Initially, the central particle is polarized by a small amount,  $1.5 \times 10^{-9}$  computational units.

(b) The mean polarization of all particles,  $\langle P \rangle$ , grows exponentially in time, at a rapid, primary, rate until the maximum polarization,  $P_{max}$ , is reached, then at a lower, secondary, rate. (c) Alternatively, if every particle is initially randomly polarized, multiple coarsening domains form: light regions have  $\langle P \rangle = P_{max}$ ; dark regions have  $\langle P \rangle = -P_{max}$ . (d) In the short term,  $\langle P \rangle$  grows exponentially with a faster rate than for the single particle case of (a)-(b).

Apparently, in the simple case without neutralization, a small initial polarization grows exponentially rapidly until the entire lattice becomes uniformly polarized. This is not mysterious: The exponential growth is a predictable consequence of the non-linear feedback produced by adding an induced polarization  $\chi_e \cdot E_i$  due to neighboring charges to every particle. Every particle obeys the same rule, so with each time step

the polarization must grow by a constant factor: A well-established formula for exponential growth. We emphasize that the  $\eta = 0$  case produces an exponential growth in polarization, but as prescribed by Eq. (2.4-2.5) no transfer in charge occurs. So every particle remains charge neutral, whereas the polarizations of each particle in a stack rapidly approach  $P_{max}$ . We will return to this point at the conclusion of this article.

To examine a more general case, instead of beginning with a single polarized charge, we investigate the lattice dynamics if we initialize the lattice by choosing each particle's charges  $Q_i^{top} = -Q_i^{bottom}$  randomly to be -1, 0, or 1. We then obtain a result as shown in Fig. 2.1(c) in which polarizations again grow exponentially rapidly so that adjacent regions almost immediately approach the maximum polarization  $\pm P_{max}$  (shown as black and beige in the figure). Thereafter, domains coarsen until a uniformly polarized state is ultimately adopted: In our simulations of 1000 particles, this takes over  $10^7$  time steps.

We turn next to the case of finite neutralization,  $\eta = 0$ , as defined by Eq. (2.4-2.5). In this case, more complex behaviors appear, summarized in the phase diagram of Fig. 2.2(a). In this diagram, we identify the dynamics observed at 10% increments of susceptibility  $\chi_e$  and neutralization  $\eta$ . For each pair of  $\chi_e$  and  $\eta$ , the state is chosen by majority vote from three trials performed using zero charge and randomized initial polarizations for every particle as well as randomly chosen collision ordering events as described previously. Criteria for establishing what pattern is present for these votes follow: In each case, the criteria are applied after a transient period of time steps needed to dissipate upward-moving waves (at least 500 time steps, in some cases up to 2000 time steps).

A uniformly polarized state is defined to have identical polarizations  $P_i = \pm P_{max}$ . This is similar to the aligned state produced by long-range ferromagnetic interactions in a 1D lattice, predicted in 1969 by Dyson [32]. In practice, as we have mentioned, we have in mind applying our lattice model to agitated granular beds, which necessarily differs from Dyson's system in several ways. First, granular beds are intrinsically nonequilibrium, so our system is not Hamiltonian. Second, dipole moments are continuous-valued

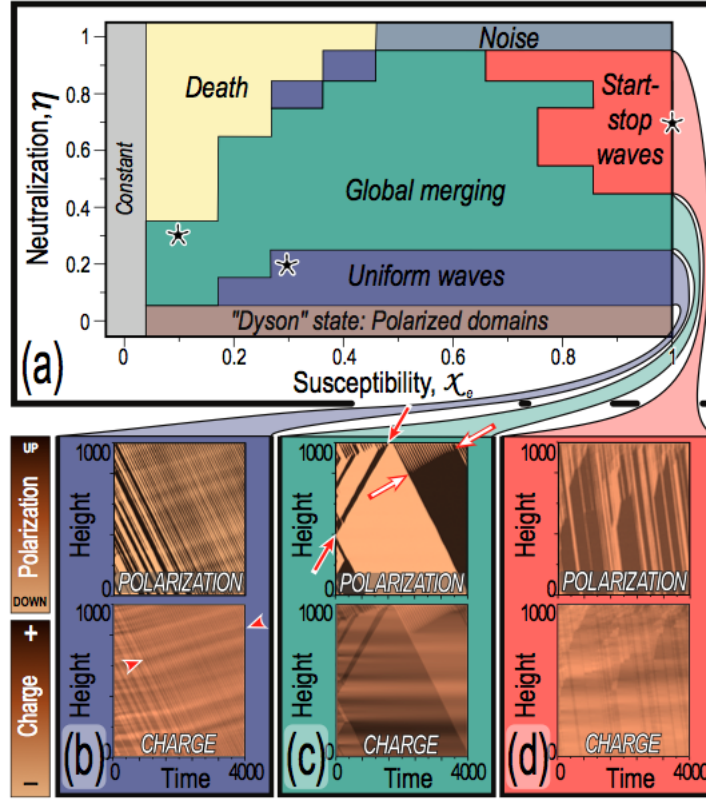


Figure 2.2: 1-D Lattice Phase Diagram.

(a) Phase diagram showing distinct spatio-temporal patterns of polarization and charge dynamics. Asterisks indicate parameter values at which spatio-temporal plots beneath are taken. (b)-(d) Color-coded plots of the polarization and charge of the 1D cellular automata (CA) lattice vs. time. Arrowheads in (b) identify upward motion of charge waves; solid arrows in (c) identify upward transient waves, and open arrows in (c) identify abrupt cooperative stopping of downward polarization waves discussed in the text.

rather than discrete. Third, as described in Eq. (1) we use both paraelectric and ferroelectric moments. Finally, technically Dyson's long-range interactions go as  $\frac{1}{r^\alpha}$  for  $1 < \alpha < 2$ , whereas our electric field  $\sim \frac{1}{r^2}$  is just outside of this range. Nevertheless, in recognition of the parallel with Dyson's earlier predictions, in Fig. 2.2 we term  $\eta = 0$  the Dyson state.

For nonzero but small neutralizations, nearly uniform downward-traveling waves of polarization  $\pm P_{max}$  appear, modulated by weak and nearly orthogonal upward-traveling

waves of charge. In this uniform waves regime shown in Fig. 2.2(b), widths of polarization waves vary by up to 50%, but fewer than five instances of merging of waves (discussed next) are seen. All simulations are performed using 1000 particles over 4000 time steps, and again every particle pair collides once during each time step: This duration was chosen because transient behaviors seen in the spatiotemporal plots of Fig. 2.2 appear to have dissipated by 4000 time steps.

As neutralization grows, increasingly irregular patterns are found. The weak modulation in downward waves [Fig. 2.2(b)] gives way at about  $\eta = 20\%$  to waves with widths that oscillate until they merge into a uniformly polarized region, and above  $\eta = 20\%$ , the merging behavior travels upward in time to produce large regions of uniform polarization as shown in Fig. 2.2(c). Polarizations again reach  $\pm P_{max}$ , and we term this a global merging state. We note that in the middle of a large lattice of particles effects of boundaries are small, and so predictably waves travel as readily upward as, downward as indicated by solid arrows in Fig. 2.2(c). Both waves die at the boundaries, but the upward waves are replaced by downward waves at the free top boundary, whereas the downward waves simply end at the grounded bottom boundary. We discuss effects of boundaries shortly.

The speed of upward merging waves, identified by open arrows in Fig. 2.2(c), is midway between the more rapid upward transient wave speed [solid arrows in Fig. 2.2(c)] and the slower upward net charge speed, identified by arrowheads in Fig. 2.2(b). We discuss wave speeds shortly but emphasize that the root causes of these three different speeds are not understood.

At still higher  $\eta$ , three additional states emerge. At low  $\chi_e$ , the lattice rapidly approaches zero charge and polarization irrespective of the initial condition: This is logical since particles are weakly coupled together but strongly neutralize. We term this state death. At  $\eta \approx 1$ , sufficiently large  $\chi_e$ 's can sustain nonzero charges, but these change rapidly and show no coherent motion: We call this noise. Finally, for large  $\chi_e$ 's and moderate  $\eta$ 's, a state emerges in which both downward-traveling waves and upward-traveling merging events are seen, each traveling at different speeds. We term this state, shown in Fig. 2.2(d), start-stop waves. The polarization here remains



small, never approaching  $P_{max}$ , but coherent traveling waves are readily identifiable. We remark that the global merging state transitions gradually to start-stop waves as  $\chi_e$  grows. As we have described, the lines demarking this transition are obtained from a majority vote of three trials, however, it is likely that another set of trials would result in slightly different transition lines.

Evidently there is a rich variety of patterns in this simple system, and these patterns exhibit several distinct traveling speeds. Despite its simplicity, the model involves two coupled and nonlinear fields, one for the net charge on each particle and one for its polarization, and from that perspective, perhaps the variety of behaviors is not surprising. We begin an analysis of these complex states by focusing on the simplest of the lattice dynamics, the uniform wave state. As shown in Fig. 2.2(b), polarization waves tend to travel down the lattice rather than up. This asymmetry can only originate from the boundaries, for within the lattice the rules for charge dynamics are entirely symmetric-and for this reason, waves can travel both up and down until they hit the boundaries [as in the example of the solid arrows of Fig. 2.2(c)]. At the boundaries, symmetry is broken: As we have mentioned, the bottom boundary is grounded, whereas the top boundary is free. Without this asymmetry, for example if both boundaries are grounded, the model produces no net transport of charge or polarization.

Behavior at the bottom boundary can easily be understood. Consider the case in which the bottom-most few particles are polarized up (with plus on top). The bottom-most charge is always zero, so the bottom particle must be net positively charged to conform with the polarized-up ansatz. This will tend to induce the next particle to be more negative below and more positive above-thus, reinforcing the up-polarized state. Consequently, the bottom boundary condition strengthens the existing polarization and cannot cause the flip in polarization seen in Fig. 2.2(b).

Since the bottom-most charge never varies from zero, let us examine the topmost charge, whose value can change as a result of induction from the field of particles beneath. Again, consider the case of up-polarized particles. Since the topmost Nth particle is induced to be polarized up, the topmost charge  $Q_N^{top}$  will be positive, and after collision all contacting charges beneath will partially neutralize. But  $Q_N^{top}$  has no

upper neighbor and so will grow monotonically due to the polarizations of particles beneath. A positive  $Q_N^{top}$  will tend to induce particles beneath to be polarized down, and since  $Q_N^{top}$  grows monotonically, at some point this topmost charge will grow until it induces the  $N - 1$ st particle to flip signs: This occurs when the field due to  $Q_N^{top}$  exceeds  $P_{max}/\chi_e$ . This begins a cascade: Once the  $N - 1$ st particle has flipped, the particle beneath (the  $N - 2$ nd particle) will be sandwiched between particles with opposite polarizations, and with  $Q_N^{top}$  positive, this too contributes to a flip of the  $N - 2$ nd particle. This, of course, is not inevitable, and as shown in Fig. 2.2, a number of other outcomes are possible; nevertheless, this appears to be the mechanism by which symmetry is broken to produce down-moving polarization waves.

We confirm that waves emanate from the top free surface of the lattice by perturbing only the topmost charge with parameters in the uniform wave regime  $\chi_e = 0.3$ ,  $\eta = 0.2$ . As shown in Figs. 2.3(a)-(c), artificially adding a positive charge to  $Q_N^{top}$  causes the polarizations beneath to prematurely flip, whereas subtracting the same charge causes the flip to be delayed. This effect is repeatable for charge injections at the top of the stack, however trials (not shown) in which equivalent charges are added to or subtracted from particles within the bed do not produce a change in polarization or charge waves. Apparently, the downward-moving polarization waves emanate from induced charges at the top of the stack of particles and are passively absorbed by the grounded bottom of the stack. Moreover, as identified by the circle in Fig. 2.3(b), pattern variations also are convected downstream by disturbances near the top of the stack-so the topmost particle affects dynamics significantly downstream as well. So the instability leading to traveling waves appears to be convective and not absolute in this system.

Evidently, the simplest dynamics, the downward-traveling polarization waves, are to some degree analytically tractable, so we continue exploiting these waves by evaluating how their wavelength  $\lambda$  and speed  $v$  depend on system parameters. Technically, we measure  $\lambda$  directly and obtain the speed using  $v = \lambda/T$ , where  $T$  is the measured wave period, and we evaluate  $\lambda$  and  $v$  during a transient period starting from random initial conditions. In this way, even if the state does not asymptotically become uniform, we can determine  $\lambda$  and  $v$ . Uncertainties inevitably result over multiple measurements,

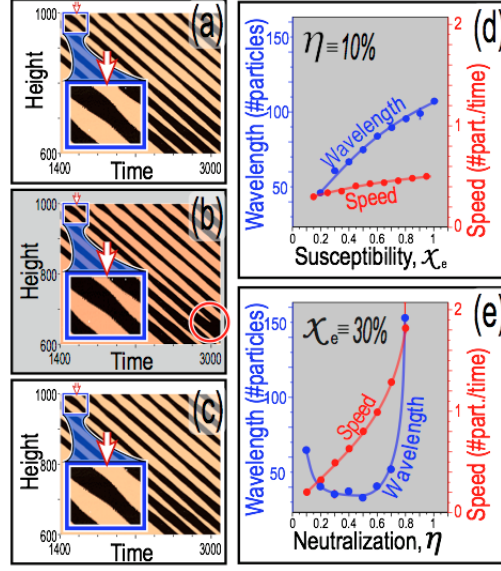


Figure 2.3: Traveling Charge and Polarization Waves.

(a) Upper portion of polarization pattern from Fig. 2.2(b). Red arrow in enlargement identifies time  $T_o = 1475$ . (b) The same pattern when a positive charge of +10 units is added to topmost particle at  $T_o = 1475$ . Notice that this provokes a premature flip from polarization up (light) to down (dark); also note that upstream perturbation causes downstream termination of the stripe (indicated by circle). (c) The same situation when a negative charge -10 is added at  $T_o = 1475$ , causing a broadening of the light stripe. (d) Wavelength and speed for  $\chi_e$  for  $\eta = 10\%$ . Note that wavelength more than doubles as  $\chi_e$  is increased, while wave speed changes by about 60%. (e) Growth in  $\eta$  increases the speed by more than an order of magnitude, but causes a nonmonotonic change in wavelength as described in text.  $\chi_e = 30\%$  in this panel.

and error bars are shown in Figs. 2.3(d)-(e), although these are typically smaller than the plot symbols.

Beginning with Fig. 2.3(d), we find that  $\lambda$  depends strongly on  $\chi_e$  at fixed  $\eta$ , more than doubling over the admissible range in  $\chi_e$ . Wave speed changes less: by about 60%. So increasing the susceptibility or coupling between particle polarizations chiefly extends the range of collective motion ( $\lambda$ ) and modestly increases the traveling speed of disturbances ( $v$ ). Particle neutralization, on the other hand, strongly affects traveling speed, increasing  $v$  by nearly an order of magnitude, as shown in Fig. 2.3(e). All of this could have been anticipated: Coupling between electric fields ( $\chi_e$ ) is bound to affect the range of particles affected by local charges, and the only way in which charges can

be transported from one location in the lattice to another is through charge transfer from one particle to another-mediated by  $\eta$ .

The effect of  $\eta$  on the wavelength shown in Fig. 2.3(e) is, however, a surprise. Apparently,  $\lambda$  grows rapidly at either low or high  $\eta$ . At low  $\eta$ , this could have been anticipated since  $\eta = 0$  must lead to the case shown in Fig. 2.1(c) in which the entire lattice is uniformly polarized. At high  $\eta$ , something else occurs: This appears to be the global merging state shown in Fig. 2.2(c). The cause of this and the start-stop waves state remains to be clarified in future studies. Likewise, the multiple different wave speeds identified by arrows in Figs. 2.2(b) and 2.2(c) are unexpected and merit further investigation.

## 2.2.5 Experimental Confirmation

### Vibrated Bed of Beads

To test whether the predicted growth in polarization occurs in real agitated beds of identical grains, we have performed experiments as follows. It is difficult to create a truly 1D experiment since agitating grains require boundaries of some kind and boundaries unavoidably produce spurious influences such as tribocharging. To minimize potential charging at boundaries, we glued  $1530 \pm 40 \mu m$  diameter glass particles inside a tall narrow (7 cm inside diameter) glass container [14], and we then filled the container to a height of 12 cm with the same glass particles and vibrated the assembly. This arrangement is not ideal-for example, the glued particles make contact only on a small area of exposed glass, whereas the free particles can make contact anywhere on their surfaces. In this context, we note that it has been known for many years that asymmetric contact between similar materials [22, 23] -for example, between a flat surface and a round particle-can generate contact charging. Nevertheless, within the constraints of what can realistically be achieved, this configuration permits us to test whether particles do polarize as expected.

In these experiments, we first dried the particles by blowing near-zero humid air (produced by a Dryex 80 air drier) for 2 minutes prior to each experimental trial.

Separate trials show humidity measured using a digital psychrometer (Extech RH300) drops to 5% relative humidity (RH) within 1 minute under these conditions. During each trial, after drying the particles we vibrate the container in a mechanical shaker at an amplitude of  $2.5 \pm 0.5\text{mm}$  and frequency of  $17 \pm 3\text{Hz}$ . The dry air is introduced through a plastic tube, and to prevent triboelectrification against the tube from generating spurious voltages, we removed the tube prior to each experimental trial.

We have performed experiments at other vibrating amplitudes and frequencies; additionally we have turned the vibration on and off multiple times to establish whether material relaxation, humidity changes, or other systematic changes occur over time. All of these tests produce similar results.

Qualitatively, we find that, provided the humidity is below RH 45%, the particles invariably stick to a grounded intruder inserted above the vibrating bed, such as a metal rod or a finger as shown in the inset of Fig. 2.4 (see also <http://link.aps.org/supplemental/10.1103/PhysRevE.89.052208>). Significantly, the grains stick to an intruder only so long as it is kept close to the vibrating bed: As the intruder is raised above the bed, the beads fall off. This indicates that the beads are kept in place by the presence of a strong electric field from the vibrating bed and not because of a persistent charge on the sticking beads themselves. Similarly, we have never observed beads to stick to the surface of the vibrating container, which we would expect if the beads became charged (cf. [25]). Since our experiment is at close to zero humidity, in a glass container on a wooden platform with no grounded surface or potential source of charge, it is not surprising that the particles do not acquire net charge. On the other hand, the apparent lack of charge on particles indicates that, despite the unavoidable nonideality of the experiment, tribocharging is not significant.

Quantitatively, we measure the voltage near of the vibrating bed as shown in the main plot of Fig. 2.4 by fixing a voltage probe above the vibrated bed and monitoring the voltage as the shaking is turned on. Measurements are taken using a Trek, Inc. (Medina, NY) model 344 voltmeter equipped with a 6000B-7C noncontact probe secured to a rod  $11 \pm 1\text{ cm}$  above the free surface of the stationary bed. At this distance, beads that bounce when the bed is vibrated never reach closer than about 2 cm from

the probe. We overlay expected results from the model described above for perfectly insulating low susceptibility particles using fit parameters  $\eta = 0$ ,  $\chi_e = 0.025$ . These experiments have been performed under a variety of conditions, including using different size and shape containers with and without glued particles. The container shape change consisted of using a convex glass vase, which has been reported to reverse or reduce granular convection; similarly, experiments were performed without glued particles because smooth boundaries reduce the extent of convection [33]. We have also performed experiments to more closely mimic our simulations in which the bottom boundary was grounded by inserting a grounded plate into the bottom of the glass container,. The data we show in Fig. 2.4 do not use a grounded bottom since a metal surface could tribocharge the glass particles, however all of these experiments produced similar results as those shown in Fig. 2.4.

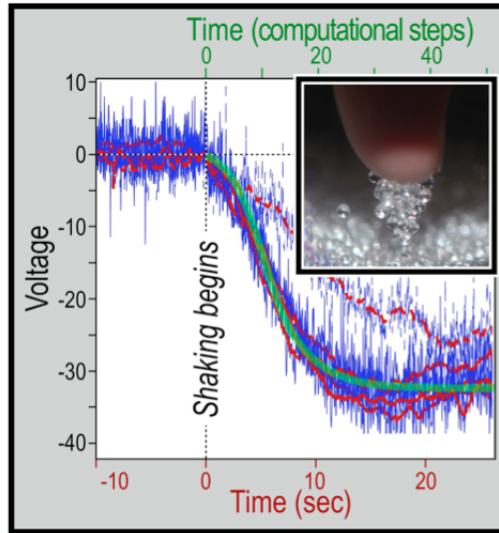


Figure 2.4: Vibrated Glass Beads Graph.

Voltage vs time from five trials in which glass beads are shaken beneath a noncontact voltage probe. The solid bold lines (red online) show running averages over 100 data points. The thick translucent line (green online) shows comparative simulation results beginning with random initial charges as in Fig. 2.2, here using  $\eta = 0$ ,  $\chi_e = 0.025$ .

We have also performed experiments using beads of different mean sizes. We find that voltages similar to those shown in Fig. 2.4 are obtained in those experiments, however beads significantly larger than the nominal  $1530 \mu m$  diameter shown in Fig. 4

(e.g., 1800  $\mu\text{m}$  beads) do not stick to an intruder, and beads significantly smaller (e.g., 630  $\mu\text{m}$  beads) stick only in a monolayer. We have not evaluated charges on individual beads as a function of size, but we interpret these results to mean that by virtue of their increased mass  $m$ , larger beads have a prohibitively large Bond number  $Bo = \frac{mg}{F_a} > 1$ , where  $g$  is gravity and  $F_a$  is the cohesive electrostatic force. Smaller beads similarly produce  $Bo > 1$  because they can sustain only a small induced polarization by virtue of their small diameters.

### Charge Imaging with Polymer Disperse Liquid Crystals

An additional type of experiment that we attempted was the use of polymer dispersed liquid crystal (PDLC's) to image the existence of charge and polarization waves. PDLC samples consist of a mixture of liquid crystal droplets with polymers. When unpolarized light is shone on PDLC it strongly scatters making the PDLC appear opaque; the liquid crystal is in a randomly ordered state. However, when exposed to an external electric field above a minimum magnitude, the liquid crystal dipole molecules twist to align with the field allowing more transmission. As a result, the PDLC becomes less opaque. This phenomenon is known as the Fréedericksz Transition [34].

Raffi Budakian and Seth Putterman [35] have demonstrated that the Fréedericksz Transition can be used to image static charges on PDLC samples. By distributing charge on a dielectric surface with a PDLC layer underneath, they showed that by applying a sufficient bias voltage they were able to induce the Fréedericksz transition. Since static external fields are easily screened by mobile charges in PDLC, Budakian and Putterman hovered a grounded spinning blade to create a changing electric field. The resulting change in opacity allowed the authors to image the existence of static electrical charge.

In our experiments, we fabricated two main types of PDLC samples: 1. PDLC sandwiched between two conducting indium tin oxide (ITO) glasses with spacers on the 10 $\mu\text{m}$  range 2. PDLC sandwiched between a dielectric material (either 25 $\mu\text{m}$  thick Kapton film or saran wrap) and a conducting ITO glass, also with  $\sim 10\mu\text{m}$  spacers. We provide more details on our PDLC fabrication methods in Appendix A.

Our PDLC samples were first observed and imaged under a microscope. We found liquid crystal droplets with sizes ranging from 10's of  $\mu\text{m}$  to 1  $\mu\text{m}$  sized droplets. The majority of droplets were on the 1  $\mu\text{m}$  size range. The 10's of  $\mu\text{m}$  droplets were found to exist on boundaries of air pockets within our samples.

Our ITO/ITO sandwiches were hooked up to a voltage supply. We found that with our samples, when applying about  $\sim 50$  V difference between the two ITO glasses, we achieved a clear opacity change. This made sense as our spacers were also on the order of about  $\sim 10$   $\mu\text{m}$  thick. Therefore we found that on the order of 1 V/ $\mu\text{m}$ , we observed a Fréedericksz transition..

Our ITO/Kapton and our ITO/Saran Wrap samples were found to respond to an external electric field. We found that by applying voltage differences on the order of hundreds to thousands of volts we observed opacity changes in our samples. The ITO/Saran Wrap films with a lower dielectric constant were found to be more responsive with a minimum threshold voltage of 300 volts while our ITO/Kapton films had a minimum of 700 volts. Our snapshots from our videos illustrates these phenomena.

In the first set of snapshots (Figure 2.5), we demonstrate that by slapping on a second ITO glass cover onto the saran wrap we achieve a fairly clear and consistent opacity change in our PDLC with an applied voltage of about 1 kV.

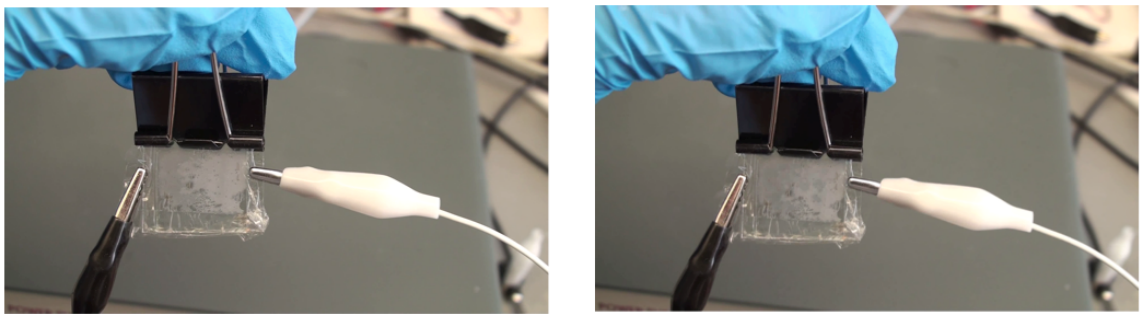


Figure 2.5: Opacity Changes in PDLC.

Right picture: Off state where there was no opacity change. Left picture: Voltage difference of 1.23 kV applied causing opacity changes.

In Figure 2.6, we show that without a second ITO glass cover we can simply touch



an alligator clip with a voltage difference of  $\sim 2.7$  kV to get an opacity change. Additionally, I turn off the voltage source to show that the opacity changes are indeed from an electric field and not from applied pressure on the saran wrap. In Putterman's paper [35], he discussed using a grounded nickel rod with a bias voltage of about 20 volts to get similar results. We have a 2 order of magnitude difference in bias voltage, but we believe this is precisely the main phenomenon discussed in his paper.

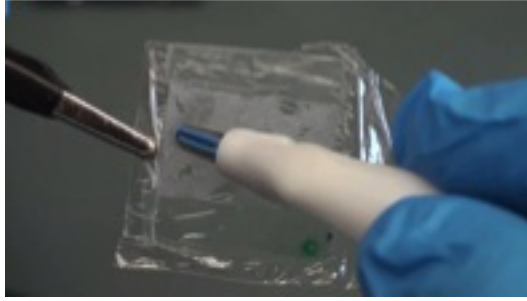


Figure 2.6: Alligator Clip Experiment.

An alligator clip with a 2.7 kV voltage difference to the ITO with the saran wrap cover. We find opacity changes corresponding to the rubbing.

Unfortunately, when placing the samples close to a static charge source in the presence of a grounded spinning blade we did not see any opacity changes. We believe that this may be due to a number of factors including PDLC thickness, distance between the grounded blade to the sample, the strength of the static charge, and also fine tuning in the bias voltage.

### 2.2.6 Concluding remarks

In conclusion, a simplified 1D model for agitated insulating particles produces a rich variety of polarized and charged states that we hope may shed light on more general cases of charging of identical materials. At its simplest, when collisions are random and insulation between agitated particles is perfect, particle polarizations grow exponentially rapidly in time, resulting in a uniformly polarized state. A simple experiment using insulating particles produces results consistent with both the uniformly polarized state and its growth.

We close by identifying several avenues for future investigation that seem to be indicated by our results. First, the model predicts that if particles are permitted to transfer charge by neutralization at their points of contact, then as described in Fig. 2.2, the uniform state should give way to traveling waves that become increasingly complex as the neutralization efficiency grows. However, such dynamic states have not yet been found experimentally. On the one hand, this may simply indicate that the neutralization  $\eta$  is very low in our experiments: A notion confirmed by the fit shown in Fig. 2.4 using  $\eta = 0$ . On the other hand, the wavelike states are a concrete prediction of the model, and future experiments engineered to more closely approximate 1D motion may reveal these states. By the same token, the 1D simplification in our model intrinsically neglects effects of particle rotation that are likely present in three-dimensional (3D) experiments, so investigations to assess how the results found in 1D change when particles rotate and interact in 3D are clearly called for.

Second, this model is restricted to the specific problem of charging of identical particles in the absence of external fields. Yet field data taken during sandstorms indicate that smaller particles tend to predominantly charge negatively [36] and that sandstorm lightning tends to occur in the presence of fields from nearby thunderstorms [8]. Expanding our model to include polydisperse particles and external fields similarly seems worth pursuing.

Third, we note that a 1D lattice of  $N$  particles with small individual polarizations  $p_i$  will cumulatively generate a total polarization  $P_{total} = \sum_{i=1}^N p_i$ , which obviously can become quite large as  $N$  grows. This leads us to speculate that voltages in excess of the Paschen breakdown limit may be achievable even in perfectly insulating particles that never individually become charged. This possibility would turn the analysis of particle charging on its head—that is, if polarization of neutral charges produces a breakdown, for example, in dry desert environments, then a breakdown could be produced in neutral grains, and charge transfer could actually follow as a result of this breakdown, rather than the breakdown occurring from particle charging as is currently assumed. This speculation seems to merit future investigation.

Finally, in all of our experiments the polarization measured is negative upwards,

so that as shown in Fig. 2.4, shaking always produces a negative voltage above the granular bed. Possibly a difference between electron states in freely moving beads at the top of the bed and trapped beads beneath causes this symmetry breaking, however precisely how this might occur also remains to be determined.

## Chapter 3

### Non-Linear Dynamics

#### 3.1 Introduction

A rite of passage for every physicist is a course intensively studying Maxwell's equations, at the level of JD Jackson's graduate text, Classical Electrodynamics. The take home lesson from this course is that because Maxwell's equations are linear, unique solutions invariably exist, so the only constraint in finding solutions by one technique or another is the doggedness of the student. Jackson mentions an important caveat, on p. 10 of his second edition [31] however, namely that once physical matter is introduced, interactions can become non-linear, at which point things become much more complex and interesting. This of course is not at all new in microscopic or quantum contexts- Kerr cells, liquid crystals, lasers and many other examples of nonlinear interactions between electromagnetic fields and matter have long been known. In this chapter, we explore lesser known effects of non-linearities at more macroscopic scales, where granular particles interact with one another- and in particular, we focus on effects of electrostatic non-linearities on particle behaviors in dust clouds. To analyze the problem, let us consider the simplest case, three particles in a line as sketched in Fig. 3.1(a). To make things even simpler, we define a fixed charge at the origin, at the top of the figure. A single uncharged test particle (Particle 1) produces no non-linearity: it becomes polarized according to:

$$\vec{P} = \chi_e \vec{E} \tag{3.1}$$

where  $\chi_e$  is the electric susceptibility, and  $\vec{E}$  is the electric field due to the fixed charge. When a second particle is introduced (Particle 2 in Fig. 3.1(a)), however, the problem becomes nonlinear. The effect of this non-linearity can be exactly calculated, leading

to a revealing outcome, as follows.

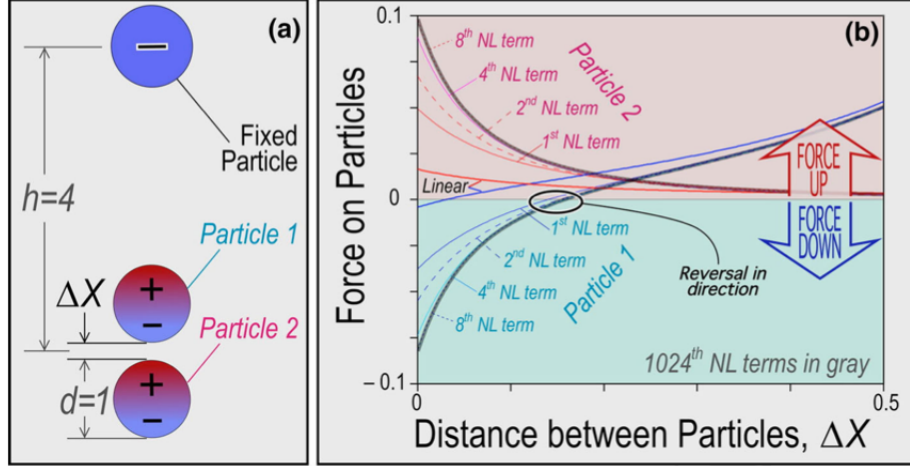


Figure 3.1: A simple two particle example of non-linearity.

Depiction of electrostatic non-linearity in its simplest context. (a) Fixed charged particle in line with two neutral test particles, each of unit diameter, separated by a distance  $\Delta X$ . Notice that each test particle polarizes, and so exerts a force on one another. (b) This mutual force, added to the force due to the fixed particle, produces a net force that causes both a quantitative change in the forces on each particle, and a qualitative reversal in even the direction of the force acting on Particle 1. These calculations use electric susceptibility  $\chi_e = 0.1$ .

Particle 2 also becomes polarized according to Eq. (3.1). From the resulting polarizations, we can calculate Coulomb forces acting on each particle: We do this by assigning fictitious positive and negative internal charges within each test particle at an arbitrary distance of  $3/4$  of a radius from the particle centers. On real particles, complex distributions of surface charges would develop [31]. We omit this realistic detail for two reasons: First because in this work we are interested in generic features associated with nonlinear interactions and not details that depend on material particulars, and second because surface charges would produce a divergence when the particles come into contact that we prefer to avoid.

Using these fictitious internal charges, we have a well defined problem: There is a fixed charge at the origin, a positive and a negative charge at known locations within Particle 1, and the same within Particle 2. Calculating net forces on the particles is straightforward, and the result is shown in Fig. 3.1(b) as a function of  $\Delta X$  (labeled

linear), where the center of mass between the two test particles is fixed (at an arbitrary distance of 4 particle diameters from the origin), and where a susceptibility of  $\chi_e = 0.1$  is used.

Careful examination of the force on Particle 1 reveals that at small  $\Delta X$  this force is negative (downward), while at large  $\Delta X$  it is positive (upward). Thus the direction of the force on this particle changes direction with its location: this is simply due to the fact that Particle 1's dipole-dipole force very close to Particle 2 overwhelms its attraction to the fixed charge.

This linear calculation, however, is incomplete, for in applying Eq. (1), we considered only the electric field due to the fixed charge, and neglected the electric field due to Particle 1. Likewise we neglected the polarizing effect of Particle 1 on Particle 2 (the so-called dipole-induced dipole effect [37]). If we use the induced charges that we have calculated to revise these dipole moments, we can re-compute the forces, producing the results identified as 1st NL term, in Fig. 3.1(b). These nonlinear corrections are themselves not complete, for like a hall of mirrors, the new polarizations produce new electric fields, which in turn induce new polarizations. It is not self-evident that this series of perturbations will converge, but as shown in Fig. 3.1(b), successive calculations up to 1024 nonlinear terms do indeed converge: in fact above about 4 nonlinear terms, the calculations reach an asymptotic value.

To confirm that this result is not geometry dependent, we have also examined a different 3 body scenario, in which the bodies are perpendicular rather than co-linear. In this case, two polarizable spheres are aligned horizontally and in contact with one another beneath a fixed charged particle, and as in Fig. 3.1(b), we evaluate the force on either dipole particle as the number of iterations of polarization calculation per timestep is increased. Again, we find that above about 4 nonlinear terms calculations reach an asymptotic value, for all heights of the fixed particle above the dipole-particles.

These calculations convey two messages that we will explore in this chapter. First, non-linear electrostatic calculations must be included to correctly evaluate forces on particles in the presence of an electric field. Indeed, when comparing the linear with the nonlinear cases shown in Fig. 3.1(b), it is evident that forces computed using linear

models can fail by more than an order of magnitude.

Second, not only can models that neglect nonlinear particle-particle electrostatic interactions fail quantitatively, they can even fail qualitatively: forces can actually reverse direction due to particle-particle interactions, and this reversal can become much more pronounced when nonlinear corrections are included in calculations (as can be seen from the 8th NL term case in Fig. 3.1(b)). Importantly, nonlinear corrections have minor influence at low particle densities (i.e. at large  $\Delta X$ ), but can dominate, or even reverse the directions of forces, at high densities.

In this chapter, we will explore experimental and computational implications of the representative calculations performed in Fig. 3.1. In Sect. 3.2, we will discuss results of a simple experiment in which dense particle clouds are exposed to electric fields, and as we will see, non-unique and fundamentally nonlinear particle behaviors result. In Sect. 3.3, we will compare these results with discrete element simulations that include Coulomb forces due to induced polarizations, and in Sect. 3.4 we will discuss the results.

## 3.2 Experiments

We have seen that non-linear electrostatic interactions between grains can become dominant at high particle densities; likewise to probe these effects it seems sensible to construct an experimental configuration that exposes grains to strong electric field gradients, so as to maximize the likelihood of encountering interesting effects. To this end, we use the apparatus illustrated in Fig. 3.2(a), which has previously been studied as a probe of dielectrophoretic effects (associated with strong field gradients) on powders and grains [38].

The apparatus consists of a nominal 30 kV Van de Graaff generator fixed beneath a grounded steel rod with a rounded end of radius 1.3 cm: this produces a concentrated electric field that polarizes and attracts particles. Particles, typically fine glass beads (details below) are placed in an insulating acrylic tray that sits on the generator. The entire system is azimuthally symmetric, so that naive electric field lines converge on the tip of the steel rod, as sketched in Fig. 3.2(a). Once agitated, particles can be

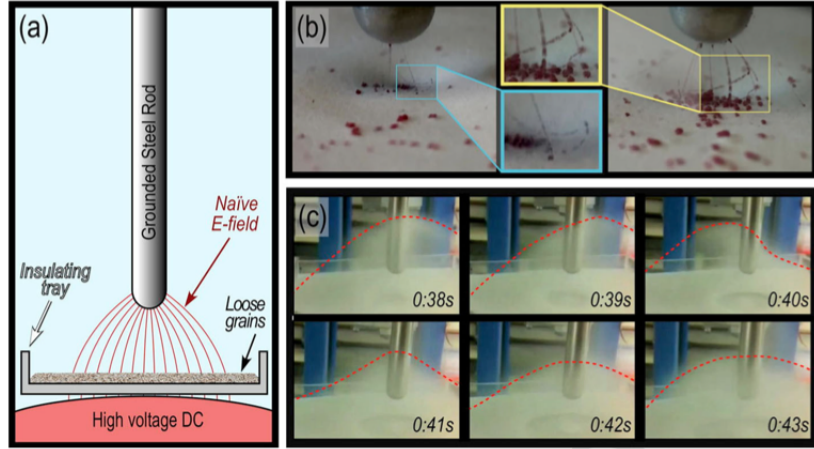


Figure 3.2: Experimental setup and results.

Experiment demonstrating effects of nonlinear electrostatic particle interactions. (a) Apparatus, consisting of grounded steel rod symmetrically placed above granular bed that is held in insulating tray, which itself sits on a high voltage Van de Graaff generator. This primarily exposes the particles to strong electric field gradients, chiefly causing polarizations and only indirectly inducing net charging. (b) Typical trajectories, in which particles (dyed red to facilitate visualization) take strongly curved trajectories that do not follow naive electric field lines (also shown in Supplemental videos 1 and 2 in Appendix B). (c) Fine glass beads that swirl around steel rod in undulating “dust devil”, following trajectories that both bear no resemblance to naive electric field lines and that vary temporally according to dynamics prescribed internally by the grains themselves and not by the steady applied field (also shown in Supplemental video 3 in Appendix B).

tribocharged or induction charged by contact with the steel rod or the acrylic tray, however there is otherwise no source of external charge, so to first order we expect particles to polarize and move radially inward toward the rod tip. Many particles do so, however many, indeed under some conditions, most do not.

This is illustrated in Fig. 3.2 (b-c). Figure 3.2(b) shows two examples of particle trajectories that are not collinear with the naive electric field, and so we infer they must be influenced by nonlinear effects. Here the bed consists of glass beads 70-110  $\mu\text{m}$  in diameter, and for visualization a subset of particles are larger and have been dyed using indelible ink. Particle trajectories over several seconds are superimposed from video records, and as highlighted in the enlargements, some colored particle trajectories travel radially along field lines as expected, but others follow very different trajectories



showing no apparent relation to the field lines. The video record (see Supplemental videos 1 and 2 in Appendix B) shows that these trajectories are substantially curved, and although not evident from these snapshots, their motions do not appear to be influenced by abrupt particle collisions or other ballistic effects rather, the motions appear to be smooth and obey complex interactions with something other than the simple field lines that we know to be present. We surmise that these motions must be associated with nonlinear influences of the other polarized (or possibly net charged) particles.

Similarly in Fig. 3.2(c), we show video frames from a cloud of similar glass beads that form a swirling cloud that undulates energetically in time. We highlight the approximate outer surface of the cloud as a broken line in Fig. 3.2(c) (visible also in Supplementary video 3 in Appendix B). Since the applied field is both spatially symmetric and temporally steady, again we surmise that the motion that we see must be associated with particleparticle interactions that appear as an indirect effect of the applied electric field.

### 3.2.1 Experimental Phase Diagram

Changing the sizes of the glass beads and varying the height of the grounded rod above the nominal surface of the granular bed produces several distinct behaviors, which we organize into a phase diagram as shown in Fig. 3.3. For each particle size and rod height, the bed was prepared at a uniform depth of 5mm, and the experiments were all conducted during a narrow period in the winter months during which the relative humidity was measured to be between 5 and 20 % using a digital psychrometer (Extech RH300). Three trials were performed for each parameter choice: typically the behavior observed was unambiguous, however in cases where non-uniqueness (discussed later) caused an ambiguity, the behavior that was observed for the majority of the three trials was taken to be the primary characteristic phenomenon.

As shown in Fig. 3.3, the smallest particles tend to form dust devils, similar to the behavior shown in Fig. 3.1(c), while the largest particles either remain stationary (in the ‘Static bed’ region) or only a small fraction are incited to jump and jostle between

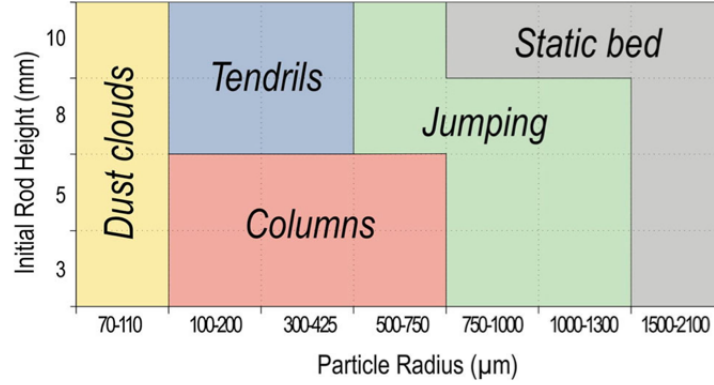


Figure 3.3: Experimental phase diagram.

Experimental phase diagram. Dust clouds refers to swirling clouds as seen in Fig.

3.2(c); Columns and Tendrils are shown in Fig. 3.7(a), 3.7(g) respectively; the Jumping state refers to particles bouncing energetically between bed and rod, and in the Static bed state, particles remain motionless, unaffected by the electric field.

bed and rod ('Jumping' region: see Supplemental video 4 in Appendix B). In the Static Bed and Jumping parameter regimes, electrical discharges from the rod to the tray are also seen- likely resulting in confounding free charges whose study we defer to the future.

The behaviors at extremes of particle sizes is predictable to the extent that they are prescribed by the Bond number,  $Bo$ -the ratio between gravitational and electrical forces. For large  $Bo$ , particles remain gravitationally bound and cannot leave the bed, while for small  $Bo$ , they are dominated by electrical forces and scarcely settle gravitationally at all. Clearly there is more to the matter than this, and we will analyze the problem further, but dynamics at the extremes is considerably less interesting than at moderate  $Bo$ , where gravitational and electrical forces are comparable.

At intermediate  $Bo$ , seen at particle radii between about 100 and 500  $\mu m$ , agitated beads tend to stick to the grounded rod, in one of two ways. For rod heights of 8 mm and above, particles cling in isolated hair-like tendrils (shown in Fig. 3.8(b) of 3.8(j)), while for smaller heights, the tendrils consolidate into growing columns that reach the particle bed (shown in Fig. 3.8(g) or Fig 3.8(h)). These columns remain stable indefinitely, and can be stretched to heights of 30 mm or greater. Typically as the column is stretched, it

thins and ultimately breaks in the center, leaving a substantial chunk of grains adhered to the rod (similar to Fig. 3.5(a)). We expect that the threshold between the jumping state and a static bed would occur at a Bond number close to one. Experimentally, this threshold occurs with beads between diameter 1000 and  $1500\mu m$ , and using the measured weight of our glass beads, we calculate the induced charge to be of order  $10^{-2}$  Coul., and the external electric field to be  $10^{-4}$  N/Coul.

### 3.3 Simulations

To confirm that these phenomena are associated with the non-linear particle-particle interactions described in Fig. 3.1, we perform simulations as follows. In principle, a comprehensive simulation of the experiments described might involve a meticulous computational reconstruction of the geometry shown in Fig. 3.2(a), including the shapes and material properties of the grounded rod, of the airborne as well as static grains in the bed, of the insulating tray, and of the surface of the Van de Graaff generator. While such a detailed simulation is surely possible, our goal here is modest: we seek to confirm the underlying mechanisms that produce the phases shown in Fig. 3.3, and for that purpose we use a comparatively simple simulation that captures the essential fields and boundary conditions that particles are exposed to, crucially allowing particles to interact nonlinearly as described in Fig. 3.1. Our philosophy in this simulation is to expose generic features at the expense of specifics—thus for example we propose that the precise shape of the Van de Graaff or tray surfaces may influence minutiae but should not substantially affect the larger dynamical behaviors seen in Figs. 3.2 and 3.3.

With this philosophy in mind, our simulation is defined using the geometry shown in Fig. 3.4(a). The Van de Graaff generator is electrically positive, and so induces negative charges at the tip of the grounded steel rod yielding zero potential at its surface, as indicated by the charges sketched in the figure. Both the surface of the generator and the rod are conductive, so their boundary conditions require normal electric fields. This makes the geometry very simple: the tip of the rod is approximately spherical. The surface of the generator is also roughly spherical, but has a much larger radius and is nearly flat on the scale of our experiment. So to a close approximation the field

lines must be as portrayed, radiating outward from the rod, and nearly vertical at the generator surface.

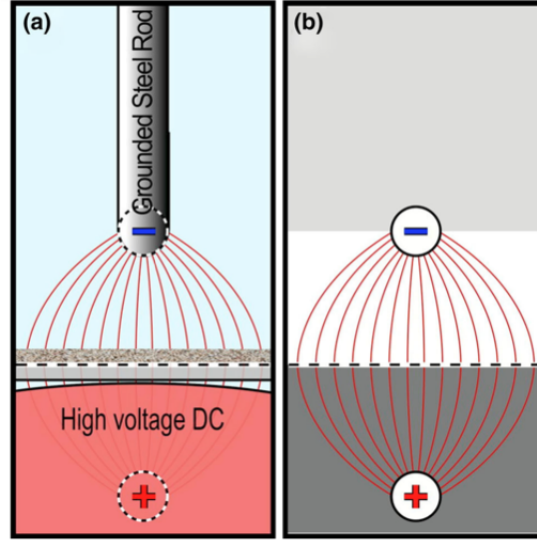


Figure 3.4: Experimental Setup vs Simulation.

- (a) Sketch of experimental geometry, with positive voltage from Van de Graaff generator and induced negative charge on tip of grounded rod indicated. (b) Equivalent system produced by an image argument, valid within the white region shown.

Geometrically, this is the same solution that one obtains from the two spherical charges shown in Fig. 3.4(b), each equally spaced from the plane of symmetry indicated by the dashed line in the figure. This result is merely a recapitulation of the argument traditionally used in the method of images, applied here to our particular problem. As always using image arguments, the solution only applies in a restricted region of space, here above the plane of symmetry and below the plane of the tip of the steel rod-thus the dark shaded region in Fig. 3.4(b) is excluded because it is within the generator (and beneath the tray) and the light shaded region is excluded because the cylindrical portion of the rod changes the field above the rod's tip. Within the white region of Fig. 3.4(b), we expect the applied field to be represented by this image argument, and as we will show, this does indeed produce results that substantially agree with experiment. We then superimpose the applied field produced from Fig. 3.4(b) on fields due to induced polarizations of all of the particles in the simulation. The particles are

taken to be polydisperse spheres, with radii that are Gaussian distributed with standard deviation of 15% of the mean radius, where we use fixed mean radius in each simulation (described subsequently) of between 0.25 and 2 computational units.

The polarizations of the particles are defined iteratively, following the rubric generalized from Fig. 3.1. That is, initially the polarizations are defined by Eq. (3.1), where  $\vec{E}$  is the external field shown in Fig. 3.4(b). We use  $\chi_e = 0.25$  for all calculations, and as in Fig. 3.1 we assign fictitious internal charges,  $q^\pm$ , at a distance 80% of the mean radius from each particle center, to produce the required polarization on each particle. These fictitious charges define a new field,

$$\vec{E}_j = \sum_{i \neq j} \frac{q_i^\pm \vec{r}_{ij}}{r_{ij}^3} \quad (3.2)$$

at each particle, denoted,  $j$ , obtained by summing over all of the other particles, indexed by  $i$ , at distances  $\vec{r}_{ij}$  from the center of the  $j$ -th charge to the  $i$ -th + or - fictitious polarized charge. Equation (3.2) is calculated for all particles and the result is added to the prior calculation of the electric field to re-evaluate Eq. (3.1) at each particle center. This process is then repeated. We discuss the number of iterations required to reach an asymptotic state shortly: for the time being, we recall that the purpose of calculating the polarizations and electric fields is to evaluate electrostatic forces on all particles. To obtain this, we note that the force on a spherical dielectric particle in a uniform electric field is zero, while the force in a non-uniform electric field,  $\vec{E}_{total}$ , is given by the dielectrophoretic formula [39].

$$\vec{F}_{Dep} = K d^3 \nabla |E_{total}|^2 \quad (3.3)$$

where  $K$  is a material constant and  $d$  is the particle diameter. We calculate the gradient by evaluating the field at the fictitious charges, giving us finally the force on each particle, due both to the applied external field and to the nonlinear interactions from neighboring, polarized, particles.

This electrical force is added to mechanical forces in a standard soft-particle discrete element method simulation described elsewhere [40], in which spheres weakly impinge

on one another during collision, and restitution forces are calculated using Walton and Braun’s longstanding method [41] with a restitution coefficient of  $\frac{1}{\sqrt{2}}$ . Except where otherwise noted, we use 500 particles in our simulations, and all particles are subjected to a gravitational body force and are constrained within a computational volume of  $50 \times 50 \times 200$  computational units. Particles that leave the top of this volume are re-injected into the simulation from below at random horizontal locations; particles that leave from the bottom or sides are reflected specularly back into the volume.

We initialize the particles by placing them at random initial locations in the bottom  $50 \times 50 \times 30$  units of the computational domain, and allowing them to settle gravitationally. In cases in which the rod tip impinges into this initial region, the height is reduced to  $50 \times 50 \times 10$  units: this causes a transient excitation due to initial effective compression of the grains, however this dissipates within the first few hundred timesteps or so of the simulation.

Experimentally, we observe that isolated particles typically bounce erratically and energetically off of the grounded rod (the Jumping state in Fig. 3.3), while groups of particles can adhere (see Fig. 3.7(f), 3.7(g)). In prior work [4], it has been observed that polarized particles vigorously recoil at odd angles from surfaces, and we speculate that this occurs due to a divergence in the Coulomb force at the instant of discharge, when the contact points of the particle and the surface share identical charge at zero separation. Whatever the cause, we model this recoil by reassigning the velocity of any particle that impinges on the rod tip to be in a random direction away from the tip and at high amplitude (we use 1500 for this value; other choices yield similar results).

This recoil applies to our observations of bouncing between bed and rod of isolated particles. We observe on the other hand that when particles near the rod are prevented from escaping by collisions with their neighbors-i.e. when particles are crowded rather than isolated-they tend to form consolidated columns, tendrils and other states shown in Fig. 3.7. We model this by increasing the coefficient of restitution by  $1/\sqrt{2}$  for every particle within 2 mean particle diameters of the rod tip. Our rationale for this modification to the code, which produces results in agreement with experimental observations, is that crowded particles that recoil from the tip will collide repeatedly

with neighbors, causing a net decrease in restitution coefficient in proportion to the number of neighbors [30]. This decrease tends to be underestimated by soft particle simulations, because the deformation of particles allows them to creep past one another more readily than is seen in practice, and the modification described produces both isolated jumping particles and consolidated groups of particles as seen in experiment.

We close this description with two final algorithmic details. First, since the particles in our experiments can be quite small and are subject to air drag, we include viscous damping in the simplest way, i.e. at every timestep ( $dt = 0.005$ ) we define

$$\vec{V} = \gamma \vec{V} \quad (3.4)$$

where  $\gamma$  is a constant (we use  $\gamma = 0.3$ ) that causes velocities to decay exponentially in time. This detail is not necessary to our results, nor is it intended to mimic effects of air currents or particle-air flow interactions, it merely causes particles to slow in a veridical manner.

Second, from Fig. 3.1 we expect to reach an asymptotic state in under 8 iterations of re-computation of the electric field described in Eqs. (3.2, 3.3), so we require that electric field is calculated 8 times without the particles moving appreciably. To achieve this, without preventing the particles from moving altogether, we demand that the simulation timestep be small enough that particles moving with the mean velocity travel no more than 10% of their diameter in 8 timesteps. This criterion is not perfect: it discounts the effect of nonlinearity on fast-moving outlier particles, however since the nonlinearity described in Fig. 3.1 is characterized by high particle density, and since particles in higher density regions typically move with lower speed, we argue that the criterion permits us to adequately model granular electrostatics in the nonlinear regime of interest. We find that this criterion appears to reproduce qualitative behaviors seen experimentally provided that the timestep is sufficiently small. For each parameter set, we reduce the timestep until further reduction no longer modifies the behaviors produced in the simulations, indicating that the simulation has converged to an asymptotic solution. Since this criterion results in quite slow effective particle motion (8 calculations of electric field and polarizations and solutions to Newton's equations of motion

for every tenth of a particle diameter moved), we reduce computational complexity slightly by using simple Euler integration to evolve particle motions. Some characteristic snapshots from our simulations are shown in Fig. 3.5. In Fig. 3.5(a-c) we show respectively an adhered cluster (a type of “tendrill” state), a steady “column” and a transient column in the process of collapsing.

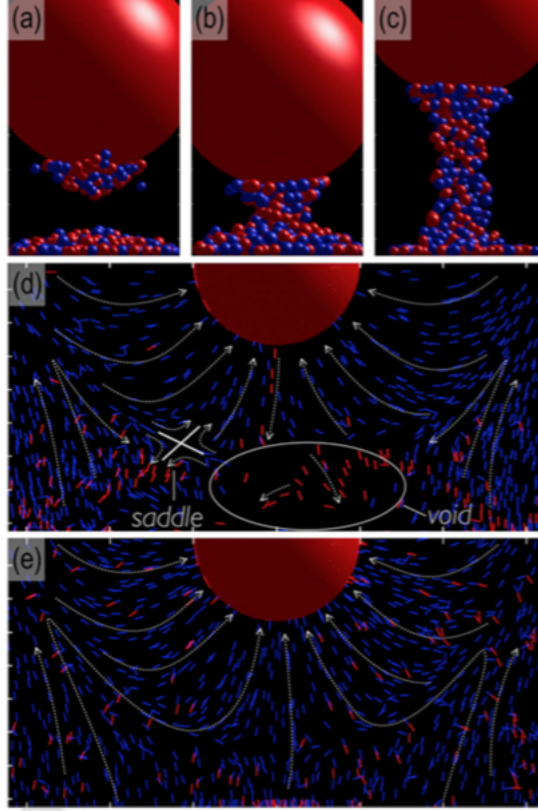


Figure 3.5: Simulation Trajectories 1.

Sample patterns seen in simulations. Snapshots from 3D simulations of (a) stable adhered cluster of particles, (b) stable column, and (c) column in the process of collapsing. Particles in a-c are shaded only to aid visualization: there is no difference between colors; a,b. are shown after 2000 timesteps, while c. is shown after 1070 timesteps: after 2000 timesteps, c produces a pendant cluster of particles as in a. (d,e) Streak lines from 2D simulations of swirling, “dust-devil”-like, flow. d and e are from the same simulation at different points in time. Blue lines indicate motion toward red rod tip; red lines travel away from the tip. White lines identify flow features described in text.

All of the simulations used to produce phases corresponding to experiment have been performed in 3D. We have also performed simulations intended to reproduce rapidly



swirling flows as in Fig. 3.2(c). In these simulations, larger numbers of particles were used, however we were not able to approach the many hundreds of thousands of airborne particles that we estimate to be present in experiments. Instead, we performed simulations of 1000 particles on 2D cross sections, as shown in Fig. 3.5(d), 3.5(e) and in Supplemental video 5 (Appendix B). This spatial domain is  $325 \times 215$  units, the tip radius is 50 units, and the mean particle diameter is 0.5 units; otherwise parameters are identical to those in the 3D simulations.

To aid visualization, we identify approximate particle trajectories as well as some notable features of the flow as white broken lines in Fig. 3.5(d), 3.5(e). Some artistic license is used in drawing these lines, and we emphasize that these are trajectories of particles and are not a smooth differential flow. Nevertheless, it is evident that the trajectories undergo temporal fluctuations in their features—thus for example there is a void at an earlier time, identified in Fig. 3.5(d), with few particles, most of which are falling downward, that is absent at a later time, Fig. 3.5(e). Likewise there appears to be a saddle point in Fig. 3.5(d) that is not evident later in Fig. 3.5(e). Thus our nonlinear simulations reproduce an overall circulatory flow along with some undulations that may be similar to those seen experimentally (cf. Fig. 3.2c and Supplemental video 3).

We note that a central tenet of our analysis is that particle motions are intrinsically non-linear due to multi-body inverse squared interactions: we recall that this led to experimental trajectories in Fig. 3.2(b) that deviate from naive field lines. We see this effect in our simulations as well. In Fig. 3.6, we show two examples of such trajectories, in which we allow 500 particles to develop into a steady state column (using mean particle radius 1.5, initial rod height 75: see Fig. 3.7), and we then eject one particle from the column by briefly delivering a large horizontal velocity to it. Such large velocities appear experimentally [4] whenever two particles in contact discharge: this causes both to instantaneously acquire identical charge at zero displacement, hence formally producing infinite repulsive force. In our simulations we don't allow charge exchange, hence we impose a large velocity instead. As shown in Fig. 3.6, both resulting trajectories are concave up, while naive field lines (Fig. 3.4(a)) are concave down.

Additionally, both trajectories break azimuthal symmetry, as shown at the tops of the two exemplars, where we show horizontal projections of the two trajectories. These projections manifestly exhibit azimuthal components of motion as indicated by black arrows. Thus in addition to circulatory flow, our simulations also produce significant deviations from naive field lines, as expected from nonlinear interactions due to nearby particle charges.

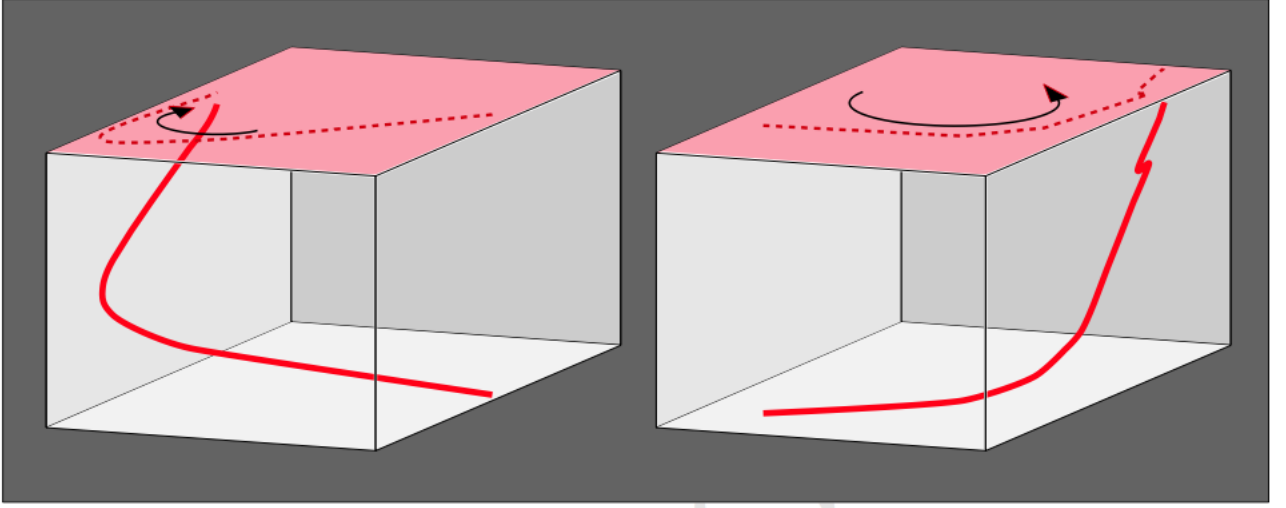


Figure 3.6: Simulation Trajectories 2.

Curved computational trajectories in which particles do not follow naive electric field lines (cf. experimental trajectories, Fig. 3.2(b)). Note trajectories are concave up, while field lines are concave down (shown in Fig. 3.2(a)), and azimuthal symmetry breaking appears in horizontal projections (dotted trajectories).

### 3.3.1 Computational Phase Diagram

We use the 3D simulation that we have described to produce a computational companion to the experimental phase diagram of Fig. 3.3. This is shown in Fig. 3.7(a), where rod heights and particle radii are varied as before. Precisely the same procedures were used as in experiment: three trials were performed for each parameter set, and the behavior assigned was determined from the majority of the trials. It is conceivable that the computational phase boundaries in Fig. 3.7(a) could depend on the convergence criterion described in the previous section that particles move on average less than

10% of their diameter in 8 timesteps. To discount this possibility and further confirm the accuracy of our simulations, we performed additional tests in which we executed 8 iterative calculations of particle polarizations for each timestep. Although more time consuming than our earlier method, this approach seems certain to generate accurate results.

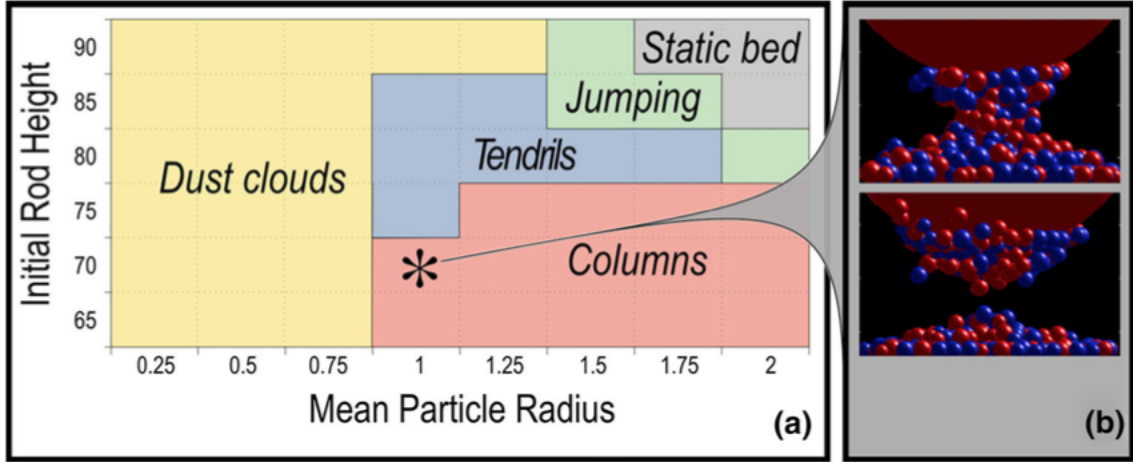


Figure 3.7: Computational Phase Diagram.

Computational phase diagram. (a) Behaviors are as described in Fig. 3.3, with the exception that fewer particles are used computationally than in experiment, so dust clouds here appear as diffusely scattering clouds of particles. (b) Asymptotic state of grains after 2000 iterates at height and radius indicated by asterisk (top panel), and under identical conditions but reducing the susceptibility as described in the text (bottom panel)

We performed these tests in two regions of phase space. First, we examined all rod heights at mean particle radii of 1 and 1.25: these radii were chosen because they produce the highest particle density and hence the strongest nonlinearity. Second, we sampled parameters in all of the five distinct states shown in Fig. 3.7(a). In all tests, we reproduced the patterns reported in that figure using the more time-consuming computational approach.

Because of the particle number limitation referred to, the patterns are not identical in experiment and simulation. For example, the Dust clouds region refers to diffusely scattering particles, rather than the clearly identifiable swirling dust devil-like behavior seen in Fig. 3.2(c), involving very large numbers of particles, and the Tendrils state

consists of pendant clumps of larger particles (also seen in experiment but not shown here) as well as the finer projections shown in Fig. 3.8(j). Aside from details that we attribute to smaller numbers of larger particles used in simulations than experiments, the patterns seen computationally largely reproduce those seen experimentally.

Most obviously, the simulations confirm the Bond number expectation described earlier for extremes of particle size, with small particles tending to become airborne in clouds and large particles tending to be immobile, either in a static bed or in a stationary column. We expect that simulations using even larger particles would only produce a static bed, however we seek to perform all simulations under common geometric conditions, and increasing the particle size further would require increasing the simulation volume.

Additionally, the simulations qualitatively reproduce the formation of other states, including columns, tendrils and jumping beads, as can be seen from a comparison between the experimental phase portrait of Fig. 3.3 and the simulation portrait of Fig. 3.7(a). The portraits exhibit similar tendencies, with columns degenerating into tendrils as the rod height grows, and jumping states emerging as the radius and height are increased.

Nevertheless, the portraits are not identical, which we ascribe to the fact remarked upon earlier that our simulations neglect particulars such as shapes and material properties of the grounded rod, the insulating tray, the Van de Graaff generator, as well as surface charges or asperities on the grains and net charges on particles. Indeed, changes in these particulars can affect the detailed locations of the phase boundaries—for example at Radius = 1, Height = 70 (asterisk in Fig. 3.8(a)) columns are reproducibly produced, as shown in the top panel of Fig. 3.8(b), but reducing the susceptibility from  $\chi_e = 0.25$  to  $\chi_e = 0.1$  instead generates a pendant tendril, as shown in the bottom panel of that figure. Thus phase boundaries depend on simulation particulars, but the relationship between the distinct phases shown in our simulations appears to be generic and agrees with experiment.

### 3.4 Discussion

#### 3.4.1 Non-uniqueness

Apparently in both experiment and simple theory, particles in electric fields produce complex and fundamentally nonlinear responses. It is well recognized that nonlinearity is a recipe for non-unique behaviors, and indeed we see multiple distinct patterns under similar conditions. A partial sampling of some of these patterns is presented in Fig. 3.8.

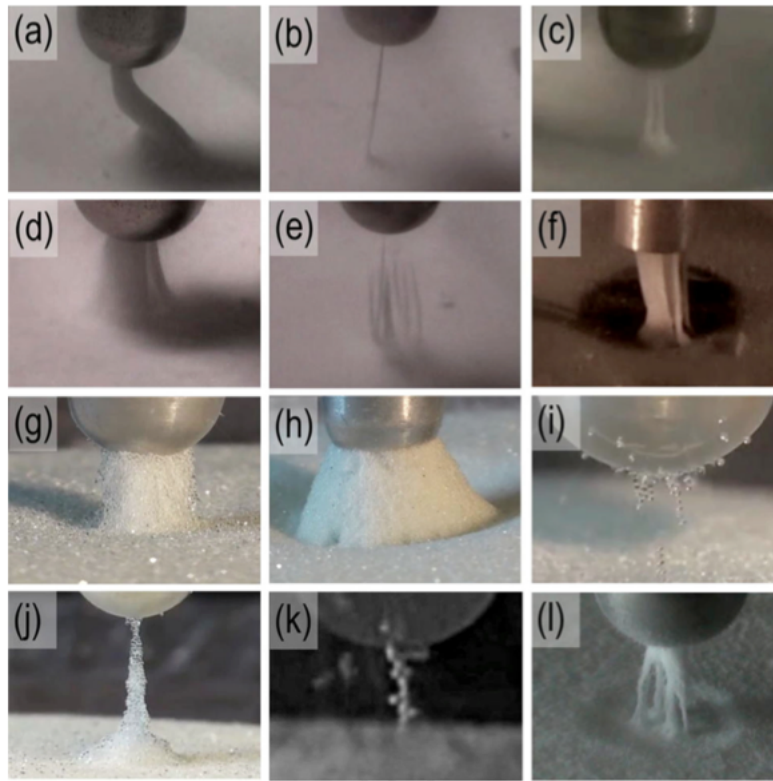


Figure 3.8: Experimental Phenomena.

Partial library of patterns near grounded rod. (a) Broad wandering column; (b) thin filament; (c) double filament; (d) dynamically dancing filaments; (e) striated ribbon beneath flat ended rod, (f) broad growing column; (g-l) a time sequence of growth and collapse of a column, (j) short tendril; (k) branched tendrils; (l) multiple steady filaments. Panels a-e use 70-110  $\mu\text{m}$  glass beads; Panels f and j use 300-425  $\mu\text{m}$  glass spheres. Panels g-i use 100-200  $\mu\text{m}$  glass spheres. Panel k uses 500  $\mu\text{m}$  zirconium oxide spheres, and panel l uses 90  $\mu\text{m}$  hollow glass spheres. Panel f is courtesy of Pinaki Chakraborty.

The examples using fine beads, Fig. 3.8(a-e), are presented roughly in order of complexity: Figure 3.8(a) shows a broad, solid column that slowly wanders as the rod is raised, this column becomes unstable, and before it disappears to produce a cloud (as in Fig. 3.2(c)), transient patterns may appear, as shown in Fig. 3.8(b-d). Several of these appear in Supplemental video 6 (Appendix B): Fig. 3.8(d) in particular shows intriguing filaments that briefly dance around one another before vanishing.

Not surprisingly, the particular patterns depend on details of the experiment, although the particulars themselves are not intuitive. For example, in Fig. 3.8(e), we show patterns beneath a flat, rather than round, ended rod: these take the appearance of ribbons rather than columns., and unlike the patterns shown elsewhere in which the grounded rod was always kept at a fixed initial height above a uniform bed, in Fig. 3.8(a-d) the grounded rod was very slowly raised from being initially immersed in the granular bed.

We have investigated various size and material grains as well; by and large we find that if the rod is further than a couple of centimeters from the bed, grains smaller than about  $100\ \mu\text{m}$  produce clouds as in Fig. 3.2(c), while larger grains tend to bounce between the bed and the rod, as in Fig. 3.2(b). This bouncing (the Jumping state referred to earlier) starts and stops in time for unexplained reasons (see Supplemental video 4). For larger beads, more intricate and dynamic structures tend to give way to more stable columns; thus  $300\text{-}425\ \mu\text{m}$  glass beads shown in Fig. 3.8(f) produce simple columns of varying widths. As the rod is brought closer, stable filaments of several varieties can form: these can take the form of single filaments, as shown in Fig. 3.8(j), 3.8(k) or multiple filaments, shown in Fig. 3.8(l) using hollow glass spheres(Q-cell 6048, PQ Corp., Augusta, GA) with mean diameter  $90\ \mu\text{m}$ . These exploratory investigations are not comprehensive, and we emphasize that even within the materials and conditions studied we encountered many unexplained behaviors. For example under similar conditions, sometimes we observed dancing columns (Fig. 3.8(d)), other times we did not. Even the more mundane, steady, behaviors showed complexity: the static column shown in Fig. 3.8(f) for example sometimes arises by slow and regular accretion, sometimes is symmetric and sometimes is not (cf. Fig. 3.8(g)), and sometimes appears

after multiple growth and collapse events (sequence 3.8(g)3.8(i); see also Supplemental video 7 in Appendix B)

### 3.4.2 Outlook

It has been known at least since the time of Poincaré that only three bodies subject to a  $1/r^2$  gravitational field behave in complex and unpredictable ways [26,37]. One would consequently expect that multi-body dynamics under gravity would be entirely erratic and unpredictable, yet in fact large numbers of gravitating particles produce unmistakably regular dynamical structures ranging from resonant planetary orbits (e.g. between Pluto and Neptune) to Saturn’s rings to intergalactic voids and super-structures involving many millions of galaxies. In retrospect, it should therefore not be surprising that multiple bodies subject to a  $1/r^2$  electrostatic field are similarly complex. The work presented here demonstrates that even neutral particles exhibit a variety of intricate and dynamic structures. It seems certain that more realistic simulations, incorporating for example charge transfer [25] or surface charge variations, will produce further surprises. It also seems likely that non-linear electrostatic interactions affect phenomena further afield from the simple geometry studied here. For example, using linear analyses, complex granular patterns both in industrial blenders [42] and on the Martian surface [4]] have been proposed to be influenced by electrostatics, and granular stick-slip events have been found to be associated with electrostatic fields [5,6,43]. It seems reasonable to expect that nonlinear effects would alter these analyses. Similarly, it seems plausible that electrostatics may substantially affect planetary dust physics, stick-slip dynamics, and industrial powder adhesion. Future work in these areas will lead to a better understanding of the response to the electrical excitation of powders-an area of importance in problems ranging from industrial dust explosions [7] to extra-terrestrial mining and exploration [4,12,13,44].

## Chapter 4

### Size segregation in the rubble-pile asteroid Itokawa

In 2005, the asteroid 25143/Itokawa was visited by the spacecraft Hayabusa [45], and was found to display strong segregation between small and large particle sizes, as shown in Fig. 4.1(a). Raised areas [46] on Itokawa are populated by boulders ranging in diameter [47, 48] from 5 to 40 m, while depressions are filled with smooth seas of smaller particles [49] ranging from fine dust to centimeter-sized pebbles [50]. It is not known how this size segregation came about, and understanding may shed light on the processes asteroids [51–53] and perhaps other bodies [54, 55] - undergo during formation and development.

This segregation has been attributed [27, 49] to the Brazil nut effect (BNE) [14], in which particles differing in size separate during sustained vertical shaking in the presence of gravity [15, 56]. In the BNE, repeated granular jamming during the upstroke followed by friction against vertical [57] boundaries during the downstroke produce a net downward flow of smaller grains with respect to their larger neighbors, leading to larger particles above smaller.

While the BNE seems likely to affect geomorphology on asteroids and elsewhere, we point out several limitations to using the BNE to explain the observed segregation on Itokawa. First, the volume of boulders on Itokawa is somewhat larger than that of fine pebbles [45, 58]. In such a case, the BNE would cause the fines to percolate beneath the boulders so that only boulders would be visible from above [59, 60]. Second, gravity is weak on such small asteroids, yet simulations have shown that under weak gravity [61], agitation velocities required to rearrange particles are very close to escape velocities [62]. Consequently under weak gravity, reliable BNE segregation will only occur if agitation and material parameters are very carefully adjusted. Third, it has been argued [63] that



the shaking that generates the BNE could be caused by collisions of the asteroid with debris [64]. However debris collisions would produce agitation in all directions, with successive collisions almost never repeating the same trajectory. Yet importantly it is known that horizontal shaking can reverse the BNE [65–67], causing larger particles to sink rather than rise. Fourth, on Itokawa there are no vertical boundaries to produce the jamming required by the BNE, and it has been shown that non-vertical boundaries can also reverse the BNE [33]. Finally, under any gravity and for any boundaries or means of agitation, boulders roll into gravitational valleys [49, 68], yet on Itokawa boulders are seen in highlands [46], while valleys are populated entirely by pebbles [48]. So if the BNE does occur on Itokawa, it would not produce visible seas of pebbles, it would occur only under narrow parametric conditions, it is unclear whether it would cause boulders to rise or to sink, and it cannot account for the lack of boulders in gravitational valleys [62].

In this chapter, we propose an alternative, and much simpler, mechanism of size segregation on rubble pile asteroids such as Itokawa. These asteroids are believed to form by self-gravitation of debris [51], and we observe that on Itokawa the volumes of gravitated pebbles and boulders are comparable (it has been estimated that 20% of Itokawa’s surface area and a few percent of its volume consists of fine particles [45, 58]). This implies that there must be overwhelmingly more small particles than large, and so most collisions that made up the asteroid must have been from small particles.

As a rough numerical estimate, if we take pebbles on Itokawa to be of order [49, 50, 69] 1 cm in diameter and boulders to be of order [47] 10 meters, the diameters would differ by factor of a thousand. If there were equal volumes of pebbles and boulders, then there would be a billion times more pebbles than boulders. This estimate can be made more conservative by 1 or 2 orders of magnitude by taking into account the smaller total volume of pebbles than boulders; nevertheless overwhelmingly more collisions with the asteroid must have been by smaller particles than by larger.

The significance of this observation is that when a pebble hits a boulder, it rebounds (as sketched in Fig. 4.1(b), whereas when it hits a sea of other pebbles, its momentum dies (Fig. 4.1(c)). This well-known consequence of inelastic collisions [70] has been

understood since Bagnold’s foundational work on granular physics [71], and is caused by the fact that every collision reduces the normal speed by a constant restitution coefficient (typically ranging from 0.5 to 0.9 depending on material and conditions). Since a pebble sea contains numerous pebbles, an incoming debris particle correspondingly causes numerous collisions, which makes granular beds excellent absorbers of impact [72, 73]. Thus simply by counting particles we can conclude that the collisions that made up Itokawa were overwhelmingly by pebbles, and since pebbles bounce off of boulders and sink into pebble seas, it is inevitable that these seas will grow. Moreover as we will show, this mechanism leads to smooth seas of pebbles in valleys and remnant pebble-free boulders on highlands.

We term the mechanism by which pebbles are repelled by boulders and absorbed by other pebbles “ballistic segregation”, to recognize prior work on ballistic aggregation [74], while distinguishing the present model from inelastic segregation models describing segregation due to velocity gradients [75], or particle properties [63].

We test this model in several ways in this chapter. As a first, qualitative, test, in Fig’s 4.1d, 4.1f we demonstrate that isolated collisions between pebbles and a large boulder rebound, leaving essentially no residual pebbles on the boulder, while multiple collisions between pebbles lead to aggregation of pebbles. In Fig. 4.1(d), we sprinkle 500 ml of 1 mm glass beads (pebbles) onto a ceramic plate (boulder - see video in Appendix C.1). We perform the sprinkling by tapping a sieve placed 50 cm above the plate. We measure that each tap releases about 1250 pebbles from an area of  $150\text{cm}^2$ , producing about one pebble per  $10\text{mm}^2$ . We have confirmed in separate experiments that this mechanism sprinkles pebbles according to a random and spatially uncorrelated distribution (see Appendix C.2). Fig. 4.1(d) shows the end of the experiment, when almost every pebble has left the plate. If instead we pour the pebbles from a beaker-again 50 cm above the plate-so that the pebbles collide with one another, we produce a growing mound as shown in Fig. 4.1(e) (see video in Appendix C.1): this snapshot is taken just before the beaker is empty so as to show the pouring, but the mound remains after pouring has stopped.

Similarly we initially place 100 ml of pebbles on the plate, shown on the left of

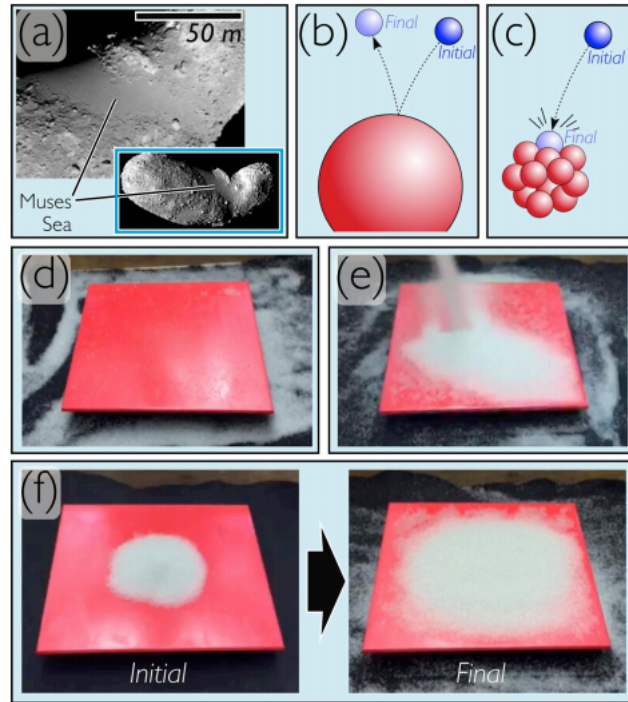


Figure 4.1: Segregation of large and small grains.

(a) Asteroid 25143/Itokawa is shown in inset; enlargement highlights size segregation, especially in the Muses sea. Credit: <http://global/JAXA.jp>. (b) Illustration of ballistic segregation: a small pebble rebounds from a larger boulder, but (c) is absorbed into a cluster of pebbles. (d) Demonstration of effect in simple experiments: small particles dropped independently onto a ceramic plate rebound leaving few residual particles, but (e) the same number of particles made to interact with one another by pouring them from the same height leave a substantial residue on the plate. (f) Similarly, if a small pile is initially placed on the plate (left), then particles sprinkled from above exactly as in panel (d) accumulate into a growing mound (right).

Fig. 4.1(f), and then sprinkle the remaining 400 ml of pebbles exactly as in panel (d), to produce a growing mound, shown to the right of panel (f) (shown also as video in Appendix C.1). So individual collisions between pebbles and a fixed boulder produce essentially no residual pebbles (Fig. 4.1(d)), while collective collisions either due to depositional conditions (Fig. 4.1(e)) or to the initial state (Fig. 4.1(f)) result in growing accumulations of pebbles.

To quantify this behavior, we reiterate that the ballistic segregation mechanism causes an incident pebble that hits an area occupied by pre-existing pebbles to accumulate. Thus existing accumulations of pebbles promote further accumulation. This

behavior is known as cooperativity [76], and is described by a Hill equation, written for our problem as:

$$F(T) = \frac{100}{1 + (k/T)^n} + f_o \quad (4.1)$$

where  $F$  defines the fraction of coverage by pebbles,  $T$  is a timescale, and  $k$  is a holding capacity. In our problem,  $T$  is the number of sieves filled with pebbles that have been deposited, and  $k$  is a timescale at which rapid filling of small interstices between boulders gives way to slow filling of large surface area seas.

Critically, the exponent  $n$  defines the cooperativity: for  $n < 1$ , pre-existing pebbles reinforce accumulation, and for  $n > 1$ , they inhibit it. We include a constant minimal coverage,  $f_o$ , to account for the observation that an initial accumulation of pebbles a seed for the pebble sea is needed to initiate cooperative behavior (shown in Fig 4.1(d) and 4.1(f)) that is, although a cluster of pebbles will absorb an incoming pebble, a monolayer of pebbles will simply be scattered by it.

To evaluate whether pebble seas grow according to the cooperative law, we perform trials in which we randomly arrange river stones, mean volume  $140 \pm 110 \text{ cm}^3$  on the bottom of a  $45 \text{ cm} \times 45 \text{ cm}$  box, and uniformly sprinkle 1 mm glass beads from a height of 50 cm as described in Appendix C.2 . We take high-resolution snapshots of the surface after depositing successive 1000 ml sieve-loads of these pebbles. We correct for camera perspective of each snapshot, also described in Appendix C.2, and use a vector path drawing tool from digital photo editing software (Intaglio) to manually circumscribe all surface areas that are occupied by more than a monolayer of pebbles. In Fig. 4.2(a), we show typical snapshots, in which the circumscribed pebble areas are false-colored. The actual pebbles are clear, which both minimizes adhesion and electrostatics [77] due to surface dyes and permits the ready exclusion of monolayers during photo editing, since monolayers of clear pebbles glitter visibly. Finally, the containing box has vertical side walls and is not of interest to us, so we measure the fraction of area occupied by pebbles divided by the total area of the largest inscribed rectangle that excludes the box.

Results of this process for 3 trials, where river stones are initially placed in different

random arrangements for each trial, are shown in Fig. 4.2(b). Data at each time (i.e. successive sieve-loads) are averaged and fit to Eq. [4.1] with correlation coefficient  $r^2 = 0.9994$ , and exponent  $n = 2.15 \pm 0.05$ . Since  $n$  is significantly above 1, depositing pebbles under gravity produces substantial cooperativity. This implies that existing pebbles promote further accumulation of pebbles.

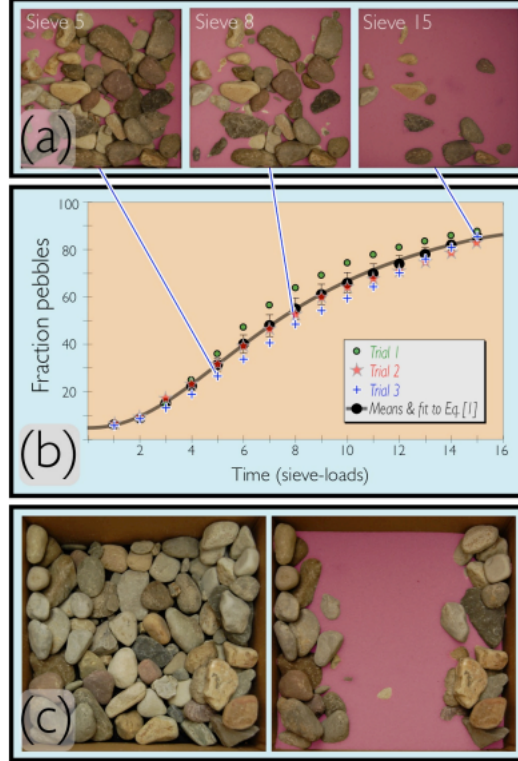


Figure 4.2: Evaluation of cooperativity in deposition of small grains. (a) Typical snapshots after sprinkling of 5, 8 and 15 sieve-loads (photos from Trial 3); small grains are false-colored to aid visualization. (b) Several trials using different initial substrates of river stones along with fit to their average from Eq. [4.1] ( $f_o = 5 \pm 1$ ,  $k = 8.0 \pm 0.2$ ,  $n = 2.15 \pm 0.06$ ,  $r^2 = 0.9994$ ). (c) In the presence of preexisting topography with a central valley, a nearly unbroken sand sea forms between higher peaks. Note that occasionally a stone may settle during an experiment, producing minor discrepancies between initial and final stone locations.

We note that surface topography i.e. substrates with substantial peaks and valleys is the rule on small asteroids, and as we have mentioned, on Itokawa pebble seas tend to form in valleys [49]. It is straightforward to repeat our experiments using a topographic substrate, with stones arranged into peaks and valleys. We have done this several

times and invariably find as shown in Fig. 4.2(c) that the valleys fill up to form nearly unbroken and flat pebble seas, leaving pebble-free stones in raised areas.

So first we calculate the surface area by setting the rate of change of volume of accumulated pebbles equal to the volume flux of added pebbles:

$$\frac{dV}{dt} = N \cdot v \quad (4.2)$$

where  $V$  is the volume of the filled valley at time  $t$ ,  $N$  is the number of pebbles added per unit time, and  $v$  is the volume of a single pebble. The simplest model for a 3D valley is a hemisphere of radius  $R$ . In this case the radius,  $r$ , of the valley at height  $h$  can be written as  $r = \sqrt{2Rh - h^2}$ . During the initial filling of a valley,  $h \ll R$ , so  $r = \sqrt{2Rh}$ , and  $V = \int \pi r^2 dh \approx \pi r^4 / (4R)$ . After integrating over time, Eq. [2] gives  $r^2 = \sqrt{4NRv/\pi} \cdot t^{1/2}$ .

Thus the surface area of a hemispheric valley initially grows as  $t^{1/2}$ . By comparison, the Hill Eq. [4.1] for short times (i.e. small  $T/k$ ) gives a fraction fill of  $[F(T) - f_o] = 100 \cdot t^n$ , where  $t=T/k$ . We have repeated this calculation for a hemicylindric valley, a V-shaped valley, and a valley surrounding a hemispheric mound by simply changing the formula for  $V$  in Eq. [4.2], and we obtain surface areas that grow as,  $t^{1/3}$ ,  $t^{1/2}$ , and  $t^{2/3}$  respectively. In all cases, for early growth of a valley we obtain exponents less than one, which are inconsistent with the positive cooperation ( $area \sim t^{2.15}$ ) that we see experimentally. We conclude that our pebble seas do not grow by downhill flow into valleys.

Second, to confirm that the cooperative growth shown in Fig. 4.2(b) occurs explicitly because pebbles bounce away from larger stones and inelastically collapse into pebble seas, we perform simulations that permit us to track trajectories, pebble by pebble, so as to quantify the extent to which pebbles bounce or collapse after each collision. The simulations also allow us to evaluate the effect of gravity on the segregation observed.

Details are provided below, but in summary we perform the simulations in two steps. First, we form an initial accumulation by dropping particles, consisting either of 1 mm pebbles or larger stones, from a fixed height onto an irregular substrate. Equal masses

of pebbles and stones are dropped over time to produce accumulations such as shown in Fig. 4.3(a) after 296,888 pebbles and 36 stones have fallen. Second, we drop pebbles onto the initial accumulation and track each pebble trajectory.

In detail, the pebbles are uniformly distributed in diameter from 0.95 to 1.05 mm and have the density of glass or granite (2.7 g/cc). Material parameters are: elastic modulus =  $10^8 Pa$ , Poisson's ratio = 0.17, and coefficients of restitution and friction = 0.5. Larger stones are produced by forming an ellipsoid of 2278 pebbles and flattening two perpendicular sides to make the stone irregularly shaped (shown in Appendix C). The particles that make up the stones are identical in size to the pebbles in the bed, and are computationally "glued" together and are not permitted to move with respect to one another, although the stone itself can move freely (see Appendix C.3). To maximize the size of the stones while minimizing the computational burden, we remove internal particles, retaining only a rigid outer shell that interacts with other particles. We compensate for hollowing out the stones by increasing the density of the shell particles to make the density of the entire stone the same as that of the individual pebbles (so the density of each particle in the shell of a stone = 9.5 g/cc).

We use Earth's gravity,  $g$ , to form an initial accumulation of particles on this substrate, as shown in Fig. 4.3(a). We use Earth's gravity to establish this initial accumulation because Itokawa's gravity is very small ( $g/10^5$ ), and using this gravity would take our simulations impractically long to accumulate particles. Once the accumulation shown has been established, we vary gravity and quantify the ballistic segregation effect as follows. First, we reduce gravity to a desired level under conditions of artificially high viscosity: viscosity is necessary purely as a numerical stratagem to prevent compressed aggregates from exploding when gravity is reduced. Second, after the initial accumulation has come to rest, we remove the artificial viscosity and deploy a number,  $N$ , of stationary pebbles at a fixed height, 160 mm above the top of the pebble bed. This is shown in Fig. 4.3(b, left) for one of the four quadrants of our simulation. We release these pebbles simultaneously under the desired gravity and track every pebble's trajectory: typical trajectories are shown in the video of Appendix C.1. We allow the pebbles to come to rest, as shown in Fig. 4.3(b, right), and evaluate lengths of the

trajectories from initial to final contact with the aggregate. As seen from this panel, the pebbles invariably come to rest in gravitational valleys, and we plot the trajectory lengths in Fig. 4.3(c).

In the main plot of Fig. 4.3(c), we show trajectory lengths of pebbles that initially strike larger stones (pebble-to-stone) alongside distances of pebbles that initially strike other pebbles (pebble-to-pebble). The ballistic segregation hypothesis holds that pebble-to-stone particles should travel much greater distances than pebble-to-pebble particles, and that both types of particles should ultimately be deposited in pebble seas. Qualitatively, this is shown in the video of Appendix C.1 and in Fig. 4.3(b, right), which displays no residual pebbles on stones. Quantitatively, our simulations confirm that pebble-to-stone particles travel about a factor of 5 further than pebble-to-pebble particles: this is shown in the main plot of Fig. 4.3(c) for Earth’s gravity,  $g$ , using  $N=702$  pebbles, and in the inset at  $g/10^5$  (approximately Itokawa’s gravity) using  $N=693$  pebbles. Simulations performed using gravity between  $g$  and  $g/10^5$ , not shown here, produce similar results. Thus our simulations appear to confirm that pebble seas grow because incoming pebbles rebound from stones but collide inelastically with other pebbles, and this finding does not appear to depend on gravity. Additionally, in both experiments and simulations we find that ballistic segregation leads to the formation of flat pebble seas in gravitational valleys.

As a final note, we emphasize that the ballistic segregation hypothesis only considers nondestructive collisions. This is appropriate for small rubble-pile asteroids that form through self-gravitation of debris and present a small cross section to high-speed projectiles that could fracture or generate large-scale rearrangements of previously deposited materials. Beyond the formation of the asteroid, our consideration of the relevant velocity scale being the escape velocity also pertains to regolith generated by the impact of micro-meteorites on boulders. Here only the ejected debris with velocity less than the escape velocity land back on the asteroid.

To estimate effects of collisions through self-gravitation, we note that Itokawa’s escape velocity is only about 0.2 m/s, and at this re-entrant speed, debris would not fracture or substantially rearrange regolith. We predict then that small rubble piles



should be subject to ballistic segregation and should generically exhibit strong segregation between small and large debris deposits. Indeed, analysis of spectroscopic [78] and thermal imaging [79] data indicate that the comparably-sized asteroid 101955 Bennu (selected for visitation in 2021 by the NASA explorer OSIRIS-REx) also exhibits size segregation, with fines smaller than 1 cm and a 10-20 m boulder on its surface.

Larger rubble piles may also undergo ballistic segregation, however their increased cross sections and re-entrant debris speeds can be expected to give rise to fracture and other complicating effects [80]. We can estimate the asteroid size at which ballistic segregation will lose its influence by observing that the specific impact energy at which chondrite [80] and similar rocks [52] fracture is above  $2 \cdot 10^6 \text{ erg/g}$ . This implies that the speed that will fracture a projectile must exceed 2000 cm/sec, which is close to the escape velocities of the asteroids 253 Mathilde or 243 Ida. We therefore predict that sand seas will grow on rubble piles smaller than these asteroids, but that ballistic segregation will give way to other effects on larger asteroids. Larger asteroids may experience ballistic segregation during their evolutions, but they will also suffer significant fracture and rearrangement, minimizing the effects of segregation over their histories.

Beyond small rubble-pile asteroids, it is enticing to note that even the large and consolidated asteroids Vesta [81] and Eros [82] possess flat ponds believed to be composed of fine particles. These deposits have been proposed to be created by a number of mechanisms including electrostatic levitation and micrometeorite abrasion. Irrespective of how the deposited particles arise, all existing models appeal to a secondary mechanism such as seismic shaking to impose flatness on the ponds [83]. Yet as we have mentioned, both experiments and simulations of ballistic segregation lead to flat deposits, and so we speculate that this effect may play a minor role in large asteroids as well.

In conclusion, we have hypothesized that rubble-pile asteroids such as Itokawa may be size segregated simply because they have accumulated debris by collisions that were predominantly, by number, by smaller particles. We have argued that the predominance of small particle collisions leads to a growth of pebble seas caused by inelasticity of collisions. We have also shown that this mechanism accounts for the formation of pebble seas in valleys and an absence of pebbles in highlands. We have performed

experiments and simulations to assess each part of this hypothesis. Experimentally, we have found that isolated pebbles that strike a large object rebound to end up far away from the object (Fig. 4.1(d)), while collisions between multiple pebbles lead to growing aggregates (Fig's 4.1(e)-(f)). We have further determined that this growth is well described by a cooperative Hill equation (Fig. 4.2). Computationally, we have evaluated distances traveled following an initial collision with either a large stone or a pebble sea, under gravities ranging from Earth's down to Itokawa's gravity, and we have confirmed that pebbles consistently rebound much larger distances from larger stones than from pebble seas. While it remains to be seen how broadly this phenomenon may be applied, we propose that the underlying mechanism is simple and general enough to be included as a process that may play a significant role in asteroid geomorphology.

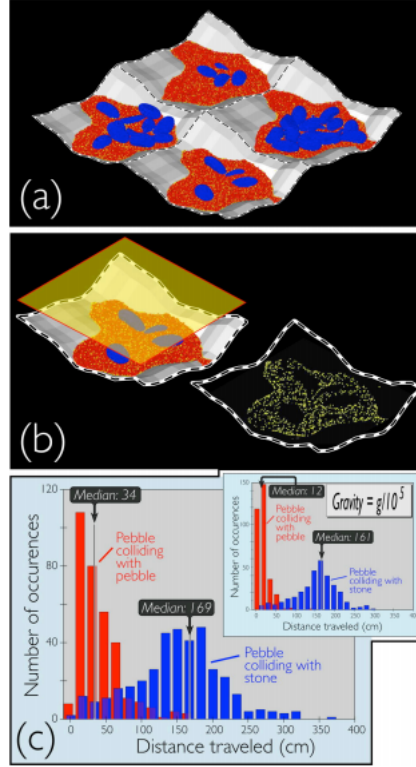


Figure 4.3: Discrete element simulations using LIGGGHTS of 1 mm diameter pebbles and larger stones dropped from fixed height but random horizontal positions onto fixed substrate.

(a) Typical result after 296,888 smaller pebbles and 36 larger stones have been dropped. The simulation is periodic in horizontal dimensions  $x$  and  $y$ , with underlying topography defined in the vertical,  $z$ , direction so as to generate a somewhat irregular substrate:  $z_{\text{substrate}} = 10 \cos(\pi x/80) + 5 \sin(\pi x/80) + 10 \cos(\pi y/80) + 2.5 \sin(3\pi y/80)$ . (b) Semi-transparent plane identifying height from which pebbles are dropped (upper image), and final locations of a large number of pebbles (lower image). (c) Lengths of trajectories, obtained from tracking a large number of pebbles (see text). Main plot shows result using Earth's gravity,  $g$ ; inset shows result using  $g/10^5$ : in both cases, pebble-to-pebble collisions are transported much shorter distances than pebble-to-stone collisions.

## Chapter 5

### Conclusion

The three projects discussed in the previous chapters provide cases of complex non-linear behavior found in granular materials along with possible theories for the mechanism behind the phenomena. The 1-d dipole lattice model with  $\frac{1}{r^2}$  interactions between dipoles in Chapter 2 finds that large scale exponential polarization can occur given a small perturbation of polarization within a lattice of dipoles. This provides a mechanism for electrical charging in large systems of identical granular particles or insulators without any requirement for an external electric field or a size difference between particles. In Chapter 3 we show that by simply applying strong electric fields to granular materials, non-linear dynamical phenomena can be observed in experimental data. We consider a system of particles under the influence of two oppositely charged external particles creating the simple field lines found in our experiment. By calculating the resulting polarization, electric fields and dielectrophoretic forces that the particles exert on one another, we are able to qualitatively recreate much of the phenomena observed in our experiments. A comparison of computational and experimental phase diagrams, with particle radii and external field distance used as parameters, finds agreement. Finally, our study of ballistic segregation provides an alternative explanation for why particle segregation exists on the asteroid 25143/Itokawa; smaller sized particles which hit a particle bed are more likely to remain while particles which hit boulders and larger rocks are more likely to bounce away. This phenomenon leaves growing sand seas and segregation based on particle size. We show simple table top experiments which demonstrate the effect of pre-existing glass bead accumulations in particle deposition. We fit our data with a non-linear Hill equation revealing that existing accumulations of glass

beads promote further accumulation. To further support our idea of ballistic segregation, we present histograms produced by simulations. The results show that pebbles colliding with boulders have a larger mean distance traveled post collision in comparison with pebble with pebble collisions.

In Chapter 2, we present a computational 1-D Ising model as a representation of vibrated beads. By considering feedback polarization between dipoles within the lattice induced by each dipole's electric field (which have interactions proportional to  $\frac{1}{r^2}$ ) we find that a single weakly polarized particle within the lattice can lead to exponential polarization growth in the whole system. In addition, when considering neutralization between neighboring dipoles, we find distinct spatiotemporal patterns including polarization and charge waves which at times start and stop sporadically, noisy states and also states classified as "death" where dipole magnitudes rapidly approach zero. We support our simulations with a tabletop experiment with a vibrated vase full of glass beads. We find that by vibrating the granular bed, we produce a voltage vs time graph with a decreasing voltage potential over time; the experimental results show agreement with our polarization state in our simulations. Our model shows that particle size differences as well as an external electric field are not necessary requirements for large scale electrical activity in granular materials.

After studying the origins of electrical charging and polarization of granular materials in Chapter 2, we examine the resulting non-linear dynamical behavior of granular materials under the effects of strong electric fields in Chapter 3. Our experimental results show that by exposing glass beads to a simple electric field, we get complex dynamical behaviors. In particular, we find particle trajectories breaking azimuthal symmetry despite having initial naive azimuthally symmetric electric field lines. In addition we find a host of different phenomena resulting from the electric field application including the formation of tendrils, dust clouds and also sporadically jumping beads. Our simulations that consider not only the initial electric field but also the resulting polarizations of the glass beads report behavior similar behavior and we find qualitative agreement with the experiment.

In Chapter 4, we consider a different complex phenomenon involving granular materials- the segregation of larger sized boulders (on the order of 10 m) from pebbles ( $\sim 1$  cm) found on the asteroid known as 25143/Itokawa. While this phenomenon has been typically attributed to the granular phenomenon known as the Brazil Nut Effect we argue that there is no known periodic shaking or vertical walls on asteroids and gravity and collisions are also isotropic. By scaling our experiments down to 1mm sized glass beads (pebbles) we find that collision differences may be responsible for granular segregation causing a non-linear fractional surface area accumulation as modeled by the Hill Equation. Further simulations confirm that pebble with pebble collisions produce distances travelled to be significantly smaller than pebble with boulder collisions. Overall this phenomenon leads to a growth of accumulations of pebbles.

We close by discussing further work that can be done to expand on the projects presented in this work. We note that our computational dipole model in chapter 2 is 1-D. We mentioned the need for 2-D and 3-D models [84] in order to get a more accurate prediction of what can be observed in experiments. Additionally, we discussed charge imaging using PDLIC's that were found to be unsuccessful. Previous work has been done using charged printer toners [28] to denote the locations of positive and negative electric charge on balloons. Also, there have existed a number of different voltage sensitive chemicals [85,86] which may allow for charge imaging. In Chapter 3, we mentioned that further work could be done in considering charge transfer between particles within our simulations. In Chapter 4, we discussed that further work should be done in considering high speed velocities of incoming dust which may cause fracture and rearrangement on asteroid surfaces.

We conclude by emphasizing the importance of each one these non-linear phenomena. Not only do the phenomena touch upon a broad range of topics including astrophysics, geophysics, engineering and meteorology, by understanding non-linear granular effects, we deepen our knowledge on industrial granular effects such as dust jamming and granular segregation. We also better understand how dust and sand particles are possibly able to build up electrical charge.

## Bibliography

- [1] H. Jaeger, S. Nagel and R. Behringer (1996) "The Physics of Granular Materials" *Physics Today* 32
- [2] A. J. Liu and S. R. Nagel (2010) The Jamming Transition and the Marginally Jammed Solid *Annual Reviews* 1:34769
- [3] T. Shinbrot (2015) "Granular chaos and mixing: Whirled in a grain of sand" *Chaos* 25
- [4] T. Shinbrot, K. LaMarche, and B. J. Glasser (2006) "Triboelectrification and Razorbacks: Geophysical Patterns Produced in Dry Grains" *Phys. Rev. Lett.* 96
- [5] T. Shinbrot, N. Kim, N. Thyagu (2012) "Electrostatic Precursors to Granular Slip Events" *PNAS* 27
- [6] K. Daniels, C. Bauer, T. Shinbrot. (2014) "Correlations between electrical and mechanical signals during granular stick-slip events" *Granular Matter* 16
- [7] K.N. Palmer (1973) "Dust Explosions and Fires" *Chapman and Hall*
- [8] AK Kamra, Visual observation of electric sparks on gypsum dunes, *Nature* 240 (1972) 143-144.
- [9] R. Anderson et. al. (1965) Electricity in Volcanic Clouds *Science* 148
- [10] R.J. Tomas et al (2007) Electrical activity during the 2006 Mount St Augustine volcanic eruptions. *Science* 315
- [11] C. Cimarelli, MA Alatorre-Ibarra, U. Kueppers, B. Scheu and DB Dingwell (2013) Experimental generation of volcanic lightning, *Geology* 1-4.
- [12] K. Kreiger (2004) "Devilish Dust Packs a Charge" *Science Now* (2004)
- [13] T.E. Bell (2006) Stronger than Dirt *Air and Space Magazine* Smithsonian (2006)
- [14] M.E. Mobius, B.E. Lauderdale, S. Nagel, H. Jaeger (2001) Brazil-nut Effect Size Separation of Granular Particles, *Nature* 429
- [15] T. Shinbrot (2004) Granular Materials: The Brazil Nut Effect in Reverse. *Nature* 352
- [16] P.F.H. Baddeley (1860) Whirlwinds and Dust Storms of India (Bell and Daldy)
- [17] E.W.B. Gill (1948) Frictional Electrification of Sand. *Nature* 240
- [18] D. J. Lacks and A. Levandovsky (2007) Effect of particle size distribution on the polarity of triboelectric charging in granular insulator systems. *J. Electrostatics* 65,

- [19] J.F Kok and D.J. Lacks (2009) Electrification of granular systems of identical insulators. *Phys. Rev. E* 79
- [20] DJ Lacks and RM Sankaran (2011) Contact electrification of insulating materials, *J. Phys. D: Applied Phys* 44
- [21] P.E. Shaw (1926) *Nature* 118
- [22] J. Lowell and W. Truscott (1986) Triboelectrification of Identical Insulators: An Experimental Investigation *Journal of Physics D: Applied Physics* 19
- [23] J. Lowell and W. Truscott (1986) Triboelectrification of Identical Insulators: Theory and Further Experiments *Journal of Physics D: Applied Physics* 19
- [24] Scott R. Waitukaitis, Victor Lee, James M. Pierson, Steven L. Forman, and Heinrich M. Jaeger (2014) *Physical Review Letters* 112
- [25] T. Pahtz, H. J. Herrmann and T. Shinbrot (2010) Why do Particle Clouds Generate Electric Charge? *Nature Physics* 6
- [26] H. Poincaré (1967) *New Methods of Celestial Mechanics*
- [27] S. Matsumura, DC Richardson, P. Michel, SR Schwartz, and RL Ballouz (2014) The Brazil-nut effect and its application to asteroids *Mon. Not R. Astron. Soc* 443
- [28] T. Shinbrot, TS Komatsu and Q. Zhao (2008), Spontaneous tribocharging of similar materials, *Europhys. Lett.* 83
- [29] MM Apodaca, PJ Wesson, KJM Bishop, MA Ratner and BA Grzybowski (2010) Contact Electrification between identical materials, *Angew. Chemie* 49
- [30] T. Shinbrot (1997), "Competition Between Randomizing Impacts and Inelastic Collisions in Granular Pattern Formation" *Nature* 389
- [31] JD Jackson (1999), *Classical Electrodynamics*, 3rd Edition *Wiley, NY*
- [32] FJ Dyson, Existence of a phase-transition in a one-dimensional Ising Ferromagnet (1969) *Commun. Math. Phys*
- [33] JB Knight, HM Jaeger and SR Nagel (1993), Vibration-Induced Size Separation in Granular Media: The Convection Connection, *Phys. Rev. Lett* 70
- [34] P.G. De Gennes and J. Prost (1995) *The Physics of Liquid Crystals*, 2nd ed *Clarendon, Oxford*
- [35] R. Budakian and S.J. Putterman (1999) Real Time Imaging of Two Dimensional Charge of Dielectric Surfaces *Review of Scientific Instruments* 71
- [36] XJ Zheng, N. Huang and YH Zhou (2003) Laboratory measurement of electrification of wind-blown sands and simulation of its effect on sand saltation movement, *J. Geophys. Res* 108
- [37] R.W. Haskell (1969) Thermodynamic model of dipole-dipole and dipole induced dipole interactions in polar mixtures. *J. Phys. Chem.* 73 628



- [38] K.R. LaMarche, F.J. Muzzio, T. Shinbrot, B.J. Glasser (2010) Granular flow and dielectrophoresis: the effect of electrostatic forces on adhesion and flow of dielectric granular materials. *Powder Technol.* 632
- [39] T. B Jones (1995) Electromechanics of Particles. Cambridge University Press, Cambridge
- [40] H.J Herrmann (1992) Simulation of granular media. *Phys. A* 191
- [41] O.R Walton, R.L Braun (1986) Viscosity, granular-temperature, and stress calculations for shearing assemblies of inelastic, frictional disks. *J. Rheol.* 30,
- [42] N.N Thyagu, A. Vasilenko, A. Voyiadjis, B. J. Glasser, T. Shinbrot (2012) Stuck in traffic: patterns of powder adhesion. *Eur. Phys. J. E* 35,
- [43] J.R. Leeman, M.M Scuderi, C. Marone, D. M. Saffer, T. Shinbrot (2014) On the origin and evolution of electrical signals during frictional stick slip in sheared granular material. *J. Geophys. Res.* 119
- [44] P. Thomas, P. Gierasch (1985) Dust devils on Mars. *Science*
- [45] H. Yano et al. (2006) Touchdown of the Hayabusa spacecraft at the Muses Sea on Itokawa, *Science* 312
- [46] OS Barnouin-Jha, AF Cheng, T. Mukai, S. Abe, N. Hirata, R. Nakamura, RW Gaskell, J. Saito and BE Clark (2008) Small-scale topography of 25143 Itokawa from the Hayabusa laser altimeter, *Icarus*, 198
- [47] J. Saito et al. (2006) Detailed images of Asteroid 25143 Itokawa from Hayabusa, *Science* 312
- [48] G. Tancredi, S. Roland and S. Bruzzone (2015) Distribution of boulders and the gravity potential on asteroid Itokawa, *Icarus* 247
- [49] H. Miyamoto et al. (2007) Regolith migration and sorting on asteroid Itokawa, *Science* 316
- [50] A. Tsuchiyama et al (2011) Three-dimensional structure of Hayabusa samples: origin and evolution of Itokawa regolith *Science* 333
- [51] E. Asphaug (2009) Growth and evolution of asteroids, *Annu. Rev. Earth Planet. Sci.* 37
- [52] E. Asphaug, EV. Ryan and MT Zuber (2002), Asteroid interiors, *Asteroids III* 1
- [53] MS Robinson, PC Thomas, J. Veverka, S. Murchie and B. Carcich (2001) The nature of ponded deposits on Eros, *Nature* 413
- [54] N. Thomas et al. (2015) The morphological diversity of comet 67P/Churyumov-Gerasimenko, *Science* 347
- [55] HF Levison, KA Kretke and MJ Duncan (2015) Growing the gas-giant planets by the gradual accumulation of pebbles, *Nature* 524

- [56] EE Ehrichs, HM Jaeger, GS Karczmar, JB Knight, VY Kuperman and SR Nagel (1995) Granular convection observed by magnetic resonance imaging, *Science* 267
- [57] HM Jaeger, SR Nagel and RP Behringer (1996) Granular solids, liquids and gases, *Rev. Mod. Phys.* 68
- [58] T. Michikami et al. (2008) Size-frequency statistics of boulders on global surface of asteroid 25143 Itokawa, *Earth, Planets and Space* 60
- [59] APJ Breu, HM Ensner, CA Kreulle and I. Rehberg (2003) "Reversing the Brazil-nut effect: competition between percolation and condensation." *Phys. Rev. Lett.* 90
- [60] JC Phillips, AJ Hogg, RR Kerswell and NJ Thomas (2006) Enhanced mobility of granular mixtures of fine and coarse particles, *Earth and Plan. Sci. Lett.* 246
- [61] G. Tancredi, A. Maciel, L. Heredia, P. Richeri and S. Nesmachnow (2012) "Granular physics in low-gravity environments using discrete element method." *Mon. Not. Royal Astro. Soc.* 420
- [62] N. Murdoch, P. Sanchez, SR Schwartz and H. Miyamoto (2015), Asteroid Surface Geophysics, *Asteroids IV*, (U. Arizona Press)
- [63] E. Asphaug, PJ King, MR Swift and MR Merrifield (2001), Brazil nuts on Eros: size-sorting of asteroid regolith, *Lunar and Planetary Science XXXII* 1708.
- [64] A. Fujiwara et al. (2006) The rubble-pile asteroid Itokawa as observed by Hayabusa, *Science* 312
- [65] PM Reis and T. Mullin, (2002) Granular segregation as a critical phenomenon, *Phys. Rev. Lett.* 89
- [66] T. Shinbrot and FJ Muzzio (March, 2000) "Nonequilibrium Patterns in Granular Mixing and Segregation," *Physics Today*
- [67] T. Schnautz, R. Brito, CA Kreulle and I. Rehberg (2005), A horizontal Brazil-nut effect and its reverse, *Phys. Rev. Lett.* 95
- [68] KM Hill and J. Kakalios (1994) Reversible axial segregation of rotating granular media, *Phys. Rev. E* 49
- [69] H. Miyamoto, JS Kargel, W. Fink and R. Furfaro (2008) Granular processes on Itokawa, a small near-Earth asteroid: Implications for resource utilization, *Proc. SPIE 6960 Space Exploration Technologies*
- [70] I. Goldhirsch and G. Zanetti (1993) Clustering instability in dissipative gases, *Phys. Rev. Lett.* 70
- [71] RA Bagnold, (2005) The physics of blown sand and desert dunes, *Dover Mineola, NY* 36
- [72] A. Sack, M. Heckel, JE Kollmer, F. Zimmer and T. Poeschel (2013) Energy Dissipation in Driven Granular Matter in the Absence of Gravity, *Phys. Rev. Lett.* 111

- [73] F. Pacheco Vzquez and S. Dorbolo (2013) Rebound of a confined granular material: combination of a bouncing ball and a granular damper, *Sci. Reports* 3
- [74] P. Meakin, P. Ramanlal, LM Sander and RC Ball (1986), Ballistic deposition on surfaces, *Phys. Rev. A* 34
- [75] JT Jenkins (1997) Particle segregation in collisional flows of inelastic spheres, *Physics of dry granular media, NATO ASI Series*, 350
- [76] AV Hill (1997) "The possible effects of the aggregation of the molecules of hmoglobin on its dissociation curves," *J. Physiol.* 40
- [77] A. Mehrotra, FJ Muzzio and T. Shinbrot (2007) Spontaneous separation of charged grains, *Phys. Rev. Lett.* 99
- [78] RP Binzel et al. (2015) Spectral slope variations for OSIRIS-REx target Asteroid (101955) Bennu: Possible evidence for a fine-grained regolith equatorial ridge, *Icarus* 256
- [79] DS. Lauretta et al (2015) The OSIRIS-REx target asteroid (101955) Bennu: Constraints on its physical, geological, and dynamical nature from astronomical observations, *Meteoritics and Plan. Sci.* 50
- [80] MJ Cintala and F. Hrzt, "Experimental Impacts into Chondritic Targets (2008) Part I: Disruption of an L6 Chondrite by Multiple Impacts," *Meteoritics and Plan. Sci.* 43
- [81] R. Jaumann et al (2012) Vesta's shape and morphology, *Science* 336
- [82] AJ Dombard, OS Barnouin, LM Prockter and PC Thomas (2010), Boulders and ponds on the Asteroid 433 Eros, *Icarus* 210
- [83] J.H. Roberts et al. (2014) Origin and Flatness of Ponds on Asteroid 433 Eros *Meteoritics and Plan. Sci.* 49
- [84] R. Yoshimatsu, N.A.M. Arajo, T. Shinbrot, H.J. Herrmann (2016) Field Driven Charging Dynamics of a Fluidized Granular Bed *arXiv:1602.03738*
- [85] Molecular Probes Handbook (2015) *Thermo Fischer Scientific* Chapter 22
- [86] J.J Garcia et al. (1998) Electrochemical Behavior of Electrodeposited Prussian Blue Films on ITO Electrode: An Attractive Laboratory Experience.: *Journal of Chemical Education* 75.
- [87] John West (1988) Phase Separation of Liquid Crystals in Polymers *Molecular Crystals and Liquid Crystals Incorporating Nonlinear Optics* 157.
- [88] O. Reynolds (1881) On the floating of drops on the surface of water depending only on the purity of the surface. *Proc. MA Lit. Phil. Soc.* 21
- [89] C. Marangoni 1870 Difesa della teoria dellelasticità superficiale dei liquidi. Plasticità superficiale. *Il Nuovo Cimento* 3

- [90] VG. Levich (1977) Physicochemical hydrodynamics, p. 754. New York, NY: Advance Publications.
- [91] LE Scriven et al. (1960) The Marangoni effects. *Nature* 187
- [92] P. Singh et al.(2009) Spontaneous dispersion of particles on liquid surfaces. *Proc. Natl Acad. Sci.* 106
- [93] PG. DeGennes et al.(2004) Capillarity and wetting phenomena: drops, bubbles, pearls, waves. New York, NY: *Springer*
- [94] MJ. Hancock et al. (2002) Fluid pipes. *J. Fluid Mech.* 466
- [95] PL. du Noüy (1925) An interfacial tensiometer for universal use. *J. Gen. Physiol.* 7
- [96] A. Assis-Jacques et al. (2006) Chemical composition of mate tea leaves (*Ilex paraguariensis*): a study of extraction techniques. *J. Sep. Sci.* 29,
- [97] RB. Bird et al. (2002) Transport phenomena, pp. 374378, 2nd edn. New York, NY: Wiley & Sons.
- [98] M. Tomczak (1988) Island wakes in deep and shallow water. *J. Geophys. Res.* 93,
- [99] WH. Hager (2012) Wilfrid Noel Bond and the Bond number. *J. Hydraulic Res.* 50
- [100] P. Tabeling (2010) Introduction to microfluidics. Oxford, UK: Oxford University Press.
- [101] A. Be'er et al. (2009) *Paenibacillus dendritiformis* bacterial colony growth depends on surfactant but not on bacterial motion. *J. Bacteriol.* 191
- [102] BD. Piorek et al. (2007) Raman spectroscopy for the optimized detection of airborne molecules. *Proc. Natl Acad. Sci. USA* 104,
- [103] JR. M. Frobisher (1926) Relations of surface tension to bacterial phenomena. *J. Infect. Dis.* 38
- [104] Q. Guo (2005) Gate and vacuum flushing of sewer sediment: laboratory testing. *J. Hydraul. Eng.* 130
- [105] RW Johnson, Handbook of fluid dynamics *CRC Press, Boca Raton, FL 1998* 5.48-5.61

## Appendix A

### Polymer Disperse Liquid Crystal (PDLC)

#### A.1 PDLC Fabrication Methods

##### A.1.1 Solvent Induced Phase Separation PDLC

Nematic liquid crystal E7 was mixed with PMMA and dissolved in methylene chloride with a 3 to 1 to 10 ratio [87]. The solution was mixed for an hour with a stir rod rotating at 400 rpm. After stirring, the solution is deposited onto a conducting indium tin oxide covered glass with spacers of a thickness of about 20 to 50 microns. The methylene chloride solvent was allowed to evaporate off and once it did, the remaining contents was heated up to 100 degrees Celsius and allowed to melt. A top layer (either another ITO glass or 25 um thick Kapton film) was then placed on top of the PDLC and pressed down to remove any air bubbles. The sample was ready once it has hardened

##### Polymer Induced Phase Separation PDLC

Nematic Liquid crystal was mixed with a monomer (Norland Optical Adhesive 65) with a 4 to 1 ratio using a stir rod rotating at 400 rpm [87]. The mixture was then deposited into an ITO/ITO sandwich, ITO/Kapton film sandwich or an ITO/saran wrap sandwich via capillary action. For spacers, we used single or double layers of saran wrap, which is known to have a thickness of 12 um, or we used 25 um thick Kapton film. The mixture was then polymerized with a black light with long wave ultraviolet wavelengths (320-400nm).

## Charge Imaging

Static charge was deposited on the dielectric using a few different objects. Following from Putterman's paper [35], a graphite tip was rubbed on the dielectric film to deposit positive charge. Negative charge was deposited on the dielectric film using an acrylic rod rubbed with faux fur or a latex balloon rubbed on one's hair. A bias voltage was then applied to the ITO glass layer to create an electric field.

In order to create a changing external electric field, a grounded spinning blade was fabricated by covering the blades of a handheld fan with aluminum foil. A wire held at ground was then touched to the axle of the fan. The fan was hovered above the PDLC sample with a distance of 1 mm or less.

## Appendix B

### Chapter 3 Supplementary Videos

Note that titles in video may show alternate numbering

- Supplementary Video 1- [http://www.edge-cdn.net/video\\_886375?playerskin=37016](http://www.edge-cdn.net/video_886375?playerskin=37016)
- Supplementary Video 2- [http://www.edge-cdn.net/video\\_886373?playerskin=37016](http://www.edge-cdn.net/video_886373?playerskin=37016)
- Supplementary Video 3- [http://www.edge-cdn.net/video\\_886377?playerskin=37016](http://www.edge-cdn.net/video_886377?playerskin=37016)
- Supplementary Video 4- [http://www.edge-cdn.net/video\\_804751?playerskin=37016](http://www.edge-cdn.net/video_804751?playerskin=37016)
- Supplementary Video 5- [http://www.edge-cdn.net/video\\_804755?playerskin=37016](http://www.edge-cdn.net/video_804755?playerskin=37016)
- Supplementary Video 6- [http://www.edge-cdn.net/video\\_886389?playerskin=37016](http://www.edge-cdn.net/video_886389?playerskin=37016)
- Supplementary Video 7- [http://www.edge-cdn.net/video\\_804753?playerskin=37016](http://www.edge-cdn.net/video_804753?playerskin=37016)

## Appendix C

### Chapter 4 Supplementary Materials

#### C.1 Supplementary Videos

- Sprinkling of beads from Fig. 4.1(d). Notice that beads rebound from ceramic plate, leaving no residue.

<https://drive.google.com/open?id=0B2sr0ZnGmkCSc3JqU3Jkc1R4Ym8>

- Pouring of beads from Fig. 4.1(e). Notice that beads collide with one another, leaving a mound on the plate.

<https://drive.google.com/open?id=0B2sr0ZnGmkCSMDV2QjhmRjUwaWM>

- Sprinkling of beads from Fig. 4.1(f). Notice that beads collide with pre-existing beads, leading to a growing mound.

<https://drive.google.com/open?id=0B2sr0ZnGmkCSZGRzZ0xvY1EyLXc>

- Simulations of pebble trajectories. Notice that pebbles colliding with pebbles do not travel far, while pebbles colliding with stones rebound greater distances.

<https://drive.google.com/open?id=0B2sr0ZnGmkCSRzFZQUV4YTl0dVE>



## C.2 Uniformity of Bead Deposition

We evaluate the spatial distribution of deposited beads as follows. We sprinkle grains onto a substrate that is divided by a plastic grid into  $1.5\text{cm} \times 1.5\text{cm}$  boxes. The substrate is wooden and is covered by a black cloth to limit bouncing and aid image analysis, and the grid effectively prevents beads from bouncing from one grid location to another. The sprinkling is performed by tapping a sieve periodically as described in the text. The sieve distributes grains onto an area of about  $15\text{cm} \times 15\text{cm}$ , so we construct a frame above the substrate and we stretch strings on the frame to subdivide it into regions of this size. We then center the sieve and sprinkle beads above each region in turn.

For the experiment in this supplement, we choose the regions sequentially, left to right, then front to back, and we change regions after 1 tap to the sieve. We evaluate uniformity after cycling through each of the 6 regions three times. In the experiments shown in Fig. 4.2, we remove any potential temporal bias by labeling regions in sequence and then choosing which region to sprinkle onto next with a random number generator. In detail, the generator randomly permutes integers up to the number of regions,  $N$ , so that every region is chosen once per  $N$  sprinkling cycles, and when  $N$  cycles have been completed, we recalculate a new random permutation so as to vary the placement of the sieve in an unbiased fashion.

Here we test uniformity by sprinkling each of 6 square regions on a  $30\text{cm} \times 45\text{cm}$  substrate. We then remove the plastic grid and photograph the deposited grains, and we perform the following image steps. First, we correct for camera perspective (using the “*unskew*” function in GraphicConverter software): this produces the figure shown in the inset of Fig. C.1. Second, we increase the contrast so that the background is entirely black and the beads are entirely white. Third, we divide the image into boxes of the same size and location as the original grid, and measure the size of a grain (15 pixels diameter). We then divide the white area in each box by the grain area to estimate the number of beads per box.

We plot a histogram of the resulting distribution of beads per box in Fig. C.1(a),

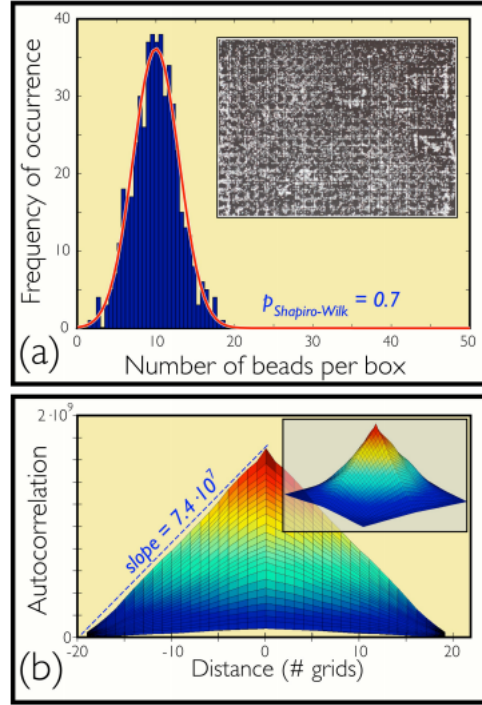


Figure C.1: Bead Deposition Graphs.

- (a) Frequency distribution within grid boxes. Inset: Beads sprinkled onto substrate subdivided into grids (see Appendix text); Main plot: histogram of number of beads per grid box, superimposed by Gaussian. (b) 2D autocorrelation of particle concentrations between boxes. Main plot: side view; inset: isometric view

and overlay this distribution with a Gaussian. To determine whether the distribution is normally distributed, we use the Shapiro-Wilk test for normality, which produces a p-value of 0.7 using significance  $\alpha = 0.05$  ( $p \gg \alpha$  implies that the distribution is highly likely to be Gaussian).

We also perform a 2D auto-correlation to evaluate spatial variations in bead concentrations, and we plot the result in Fig. C.1(b). As indicated by the dashed line, the auto-correlation drops off linearly with distance from the origin with slope  $7.4 \cdot 10^7$ . The linearity of the auto-correlation means that boxes are strongly correlated with themselves; the slope means that correlations diminish by nearly a factor of 108 from one grid box to its neighbor.

Based on the Shapiro-Wilk and correlation tests, we conclude that particles are

highly likely to be distributed within each box according to a Gaussian, and the correlation from box to box is extremely small.

### C.3 Computational Boulder Shape

Two views of computational “boulders” consisting of an ellipsoid of 2278 pebbles with two sides flattened as described in text.

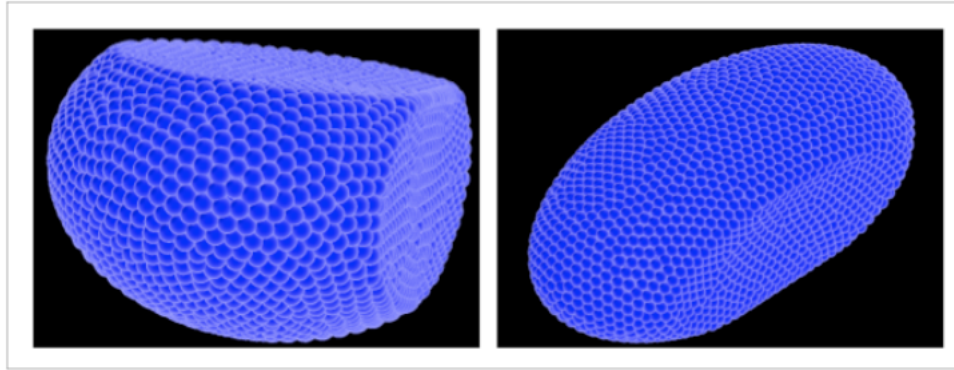


Figure C.2: Shape of computational boulders.

## Appendix D

### Upstream Contamination by Floating Particles

#### D.1 Upstream Contamination

When water is poured into a teacup, it seems self-evident that material in the cup will not make its way upstream into the teapot. Similarly, when chemicals are pipetted onto a culture plate, it is taken for granted that cells from the plate will not contaminate the chemical source. In this chapter, we demonstrate that contrary to expectation, floating particles can contaminate upstream reservoirs by travelling in rapid jets at accelerations substantially larger than the gravitational downstream acceleration. This counterintuitive phenomenon was first observed during the preparation of mate tea, when hot water was poured from a pot into a cup containing tea leaves: it was found that when the spout was within 1cm above the leaves, floating leaves would find their way from the cup into the pot (see figure D.4).

To study the phenomenon under controlled conditions, we first perform the experiment illustrated in figure D.1(a), where water flows from an upstream reservoir down an inclined channel, off a waterfall and into a receiving vessel. Floating particles of mate tea (*Ilex paraguariensis*), chalk and other powders in the receiving vessel are observed to travel up the waterfall and through the channel to end up in the upstream reservoir, as shown in figure D.1(b) (see also section D.2, video S1). The downstream water flux has been varied up to  $16\text{cm}^3\text{s}^{-1}$  along an 8cm long channel inclined at a slight angle. Experiments using inclined (figure D.1(b)) and horizontal (figure D.1(d)) channels both generate upstream contamination; effects of channel angle are discussed shortly. The snapshots shown in figure D.1 use deionized water, but experiments using tap water yield indistinguishable results; similarly, the upstream flow of floating particles persists in experiments using either boiling or cold water, and tests using fluorescein powder

also exhibit upstream contamination.

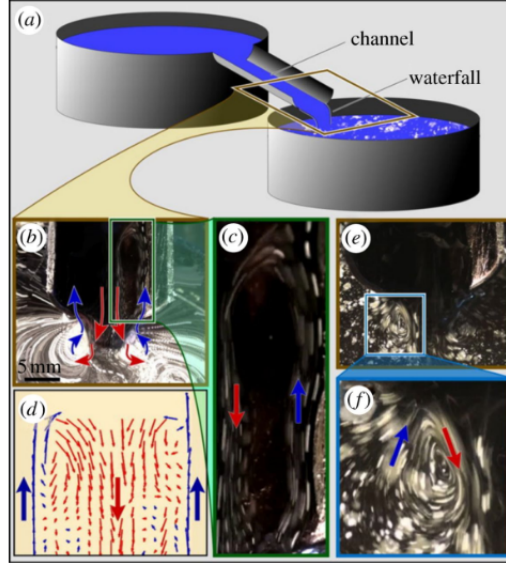


Figure D.1: Upstream Contamination Experiment

(a) Schematic showing an upstream tank containing deionized water and a downstream tank containing the same water sprinkled with floating particles. Levels of each container are independently controlled by inlet and outlet plumbing (not shown). (b) Superposition of 30 consecutive video frames (see section D.2, video S1) in a channel inclined about 20 degrees to the horizontal. Chalk on the right half of the channel flow is illuminated; chalk on the left half is present, but is in shadow. As indicated by arrows, particles travel up the back of the waterfall and the sides of the channel, and down the centre of the channel and the front of the waterfall. (c) Enlargement showing circulating particles in the channel, including one particle furthest to the right that leaves the picture frame at about  $7\text{cm s}^{-1}$ . (d) PTV of floating mate tea particles across a horizontal channel near the top of the channel at a net flow of  $16 \pm 2\text{cm}^3\text{s}^{-1}$ . (e) Snapshot of waterfall. (f) Enlargement of rapidly recirculating chalk particles, with upflow at back of waterfall and downflow at its front indicated by arrows.

The flows of particles in the waterfall and channel regions are indicated by arrows in figure D.1(b) and consist of vortices that transport particles upward from the back of the waterfall to the outside of the channel, and then back downwards through the centre of the channel and the front of the waterfall. We dissect the flows in greater detail later.

Upstream flow begins near the waterfall, shown in the snapshot of figure D.1(e) and enlarged in figure D.1(f). From these panels, we see that a pair of particle-rich

circulatory vortices form, one on either side of the waterfall (see also section D.2, video S1). Floating particles travel at speeds ranging between 1 and  $7\text{cm s}^{-1}$ , as determined by measuring the lengths of streaklines at a known shutter speed (here, 1/60s).

Only a fraction of the particles in the recirculating waterfall flow become entrained into the channel region (figure D.1(b,c)), and consequently in this region we see much lower particle densities. For this reason, figure D.1(e) contains a single snapshot, whereas figure D.1(b) requires 30 successive video frames to show a similar number of particles. As indicated by arrows in figure D.1(c), particles in the channel travel upstream near the flow boundaries, and most particles ultimately change direction and travel down the centre of the stream. Particles here travel at speeds between 4 and  $7\text{cm s}^{-1}$ , measured as before.

We have also quantified velocities using particle tracking velocimetry (PTV). Typical results are shown in figure D.1(d) from an experiment using a horizontal channel. To perform PTV, we use a horizontal channel because this generates slower downstream flow than inclined channels, and this slower speed results in longer and steadier upstream flows, which in turn produce low noise velocimetry data. Flow in a horizontal channel is produced by maintaining a slight head between the upstream and downstream reservoirs. Particle tracking of video images is performed using ImageJ software with the MTrack2 plug-in. Particle tracking confirms the visual appearance that particulate flow is predominantly parallel to the channel walls, upstream in high-speed jets near the channel edges and downstream through the channel centre.

To analyse possible mechanisms underlying the unexpected upstream flows that we report, we begin by noting that it is well established that surface tension depends strongly on the concentration of floating contaminants [88–92]. We therefore hypothesize that the higher surface tension in the clean, upper, reservoir may draw particles from the contaminated, lower, reservoir [93] against the downstream flow. Indeed, it has previously been reported that amphiphilic surfactants in a receiving reservoir can be drawn up waterfalls to a height of 2cm through surface tension gradients based on a similar mechanism [94]. Consequently, we measured the surface tension of water as a function of density of floating chalk and mate tea particles (figure D.2(a)). The chalk

particles were prepared by rubbing a stick of chalk on rough sandpaper, whereas the tea was obtained directly from commercial yerba mate leaves passed through a no. 25 (0.7mm) sieve. The chalk or mate was dropped from a small distance onto clean tap water and allowed to equilibrate, after which the surface tension was measured using the du Noüy ring method [95]. As shown in figure D.2(a), the surface tension of water decreases by nearly a factor of 2 with added chalk, and by a factor of 3 with tea. We note that the upstream contamination effect appears for both soluble and insoluble surfactants. For example, the principal ingredient in chalk, calcium carbonate, is nearly insoluble in water (solubility  $0.01\text{gl}^{-1}$  at room temperature), while we have also verified that pure fluorescein and sodium dodecyl sulfate (SDS) surfactant powder exhibit upstream contamination, with solubilities ranging from weakly to highly soluble ( $0.8\text{gl}^{-1}$  for fluorescein to  $250\text{gl}^{-1}$  for SDS).



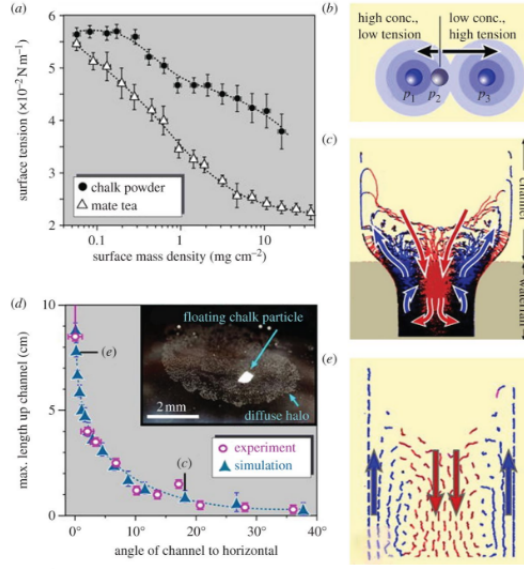


Figure D.2: Proposed mechanism for upstream contamination.

(a) Decrease in surface tension of tap water with increase in concentration of two surface contaminants studied here. (b) Cartoon illustrating reduced surface tension due to Gaussian concentrations surrounding two nearby particles. Tension is strongly reduced by a nearby particle,  $p_1$ , and is more weakly reduced by a more distant particle,  $p_3$ ; see text. (c) Simulated flow field of particles on a two-dimensional elastic surface subjected to competition between downstream advection and a surface tension gradient due to neighbours, as described in the text. Particle flow is shown by superimposing multiple instantaneous snapshots, and flow directions are indicated by arrows as in figure D.1(d). (d) Comparison between experimental and computational maximum upstream contamination distances of particles initially located in the downstream reservoir. Inset shows floating chalk particle surrounded by a diffuse halo of finer powder; the scale bar is approximate. (e) Simulated particle motion in a channel region for a shallow inclination; flow beneath this region is similar to (c). Calculated inclinations (see section D.5 for derivation) for (c) and (e) are identified in the plot of (d).

We can easily estimate the order of magnitude effect of such a change in surface tension on a floating particle, as follows. A particle of radius  $r$  on the surface of the receiving reservoir that is ideally exposed to clean water from the waterfall on one side and a fixed concentration of solids on its opposite side will feel a surface tension difference  $\Delta T$ , which from figure D.2(b) is on the order of  $0.01 \text{ N m}^{-1}$ . The resulting acceleration of the particle will be  $\Delta T \cdot L/m$ , where  $L$  is the characteristic length of a particle, and  $m$  is its mass. Taking  $L = 2r$  and  $m = 4\pi\rho r^3/3$ , where  $\rho$  is the particle

density, gives an acceleration,  $a = 10 \times 2 \times 3/4\pi\rho r^2 \sim 5/(\rho r^2)$ . A conservative estimate for  $a$  can be obtained by considering a chalk particle with bulk density  $\rho = 2.5\text{gcm}^{-3}$  and radius  $r \sim 100\text{m}$ : this gives an acceleration  $a \sim 20000\text{cms}^{-2}$ , or about 20 times gravity. This estimate should be viewed as an upper bound: most particles will likely feel a milder concentration gradient than this approximation suggests. Furthermore, it remains to be established how small the particle concentration needs to be to generate upstream contamination; however, this estimate illustrates that surface tension gradients produced by flowing clean into particulate-contaminated water can provide ample accelerations to drive particles upstream much faster than gravity. This is in keeping with more detailed calculations [94], as well as with experimental data demonstrating that fine particles disperse explosively when dropped onto a clean water surface [90].

We challenge the hypothesis that upstream contamination is driven by surface tension gradients by introducing a small amount of liquid surfactant, benzalkonium chloride, to the upper or lower reservoir. As expected, when surfactant is added to the upper reservoir, upstream contamination is abruptly eliminated, while adding surfactant to the lower reservoir causes a transient expansion of the surface layer that initiates upstream contamination if it has not yet begun, or accelerates contamination if it is already present.

To more systematically evaluate whether surface tension gradients account for the observations, we have constructed a simulation of multiple point particles on a two-dimensional domain, where each particle is subject to a competition between two influences: surface elasticity drawing particles upstream, and ambient fluid flow entraining particles downstream. Details are presented in the supplementary material in later parts of this chapter; in overview, elasticity and ambient fluid flow that drive particle motion are defined as follows.

The elasticity acting on a floating particle is taken to depend on the concentration gradient of contaminants that is produced by neighbouring floating particles. Heuristically, we model each particle as being surrounded by a halo of molecules that diminish the local surface tension between that particle and any neighbour. For example, in the inset to figure D.2(d), we confirm that a halo of fine particulates appears shortly (under

1s) after a single particle of chalk is dropped into clean water; some powders may well also contain chemical surfactants (e.g. stearic acid [96] in mate tea).

A cartoon illustrating how this heuristic is used to compute tensile forces in our simulation is shown in figure D.2(b) in the simplest case of three particles in a line, with particle  $p_1$  closer to the central particle than particle  $p_3$ . We make use of the fact that the molecular concentration surrounding a spherical source particle is analytically known [97] to be a Gaussian function of radius with prescribed variance,  $\sigma_g^2$ , and amplitude,  $A_g$ , so if we assume that all particles are identical spheres and that all Gaussians are defined at the same instant in time, we can solve for the concentration everywhere. In figure D.2(b), the contaminant concentration at the central particle,  $p_2$ , due to the Gaussian surrounding  $p_1$  would be larger than the concentration due to the more distant  $p_3$ , and consequently the elastic tension due to  $p_1$  would be smaller than that due to  $p_3$ -resulting in a net elastic force on  $p_2$  towards  $p_3$ . For simplicity, we take the surface tension to decrease linearly with concentration, and since the diffusion equation itself is linear, all concentrations-and so tensile forces-at any point are simple linear superpositions of values due to all other particles. Thus, we determine the tensile force on any given particle by evaluating the concentrations at that location due to the analytically defined diffuse halo of concentrations surrounding all neighbouring particles.

The ambient fluid velocity is calculated independently, using separate calculations in the channel and in the waterfall regions. In the channel region, surface flow is bounded at the sides, and since the shallow water Reynolds number [98] is under about 8 (see section D.5), we take the velocity at the surface in that region to be defined by laminar two-dimensional Poiseuille flow with maximum speed,  $V_{max}$ , at the centre of the channel. In the waterfall region, flow is azimuthally periodic, and so the velocity is readily expressed as a Fourier series. We approximate the flow in the waterfall to be the leading order term in this series, a single cosine, fastest in the front of the waterfall where the surface is free and slowest in its back, where the surface is initially retarded by contact with the channel. We close the problem by noting that the waterfall is fed from the channel, so that if we conserve surface area, the surface flow rate integrated across

the channel will equal the flow rate integrated around the circumference of the waterfall. This sets the amplitude of the cosinusoidal waterfall flow to be expressible in terms of  $V_{max}$ , thus reducing the number of parameters to three kinetic terms,  $V_{max}$ ,  $A_g$  and  $\sigma_g^2$ , several purely geometric terms (e.g. the widths and lengths of the channel and waterfall) and the number of particles in the simulation. Finally, we define boundary conditions by assuming that particles that impinge on the channel sides reflect specularly, whereas particles travel freely around the azimuthally periodic waterfall. Effects of parameter variations are discussed below; for further discussion, see section D.5l.

Given a choice of parameters, we calculate trajectories of particles on the surface by applying the elastic force to every particle, taken to have unit mass, and then requiring each particle to follow the ambient fluid velocity. To mimic experimental conditions, particles start in a  $1 \times 1$  unit reservoir at the bottom of the computational domain, i.e. at  $y < 0$ , and particles move on a domain  $x \in [-1, 1]$  and  $y \in [-1, \infty]$ , thereafter. To add verisimilitude, the waterfall region is defined to be narrower than the channel region (again defined in the section D.5), as shown in figure D.2(c), although separate computational trials show that geometric details such as this have little effect on the upstream contamination. Likewise, the simulations shown here use 500 particles, but we obtain similar results using between 100 and 1500 particles, with more particles crowding to move upstream as the number of total particles is increased.

More detailed embellishments to this model are certainly possible, for example, accounting for time variations in contaminant concentration surrounding each particle, or including inertial corrections. Despite its simplicity, the model captures both quantitative and qualitative features seen in experiments. Qualitatively, the model reproduces both the rapid vortical motion circulating particles between the front and back of the waterfall seen in experiments, and the upstream flow that entrains a fraction of these circulating particles to flow upstream along the edges of the channel and downstream near its centre (see section D.2 video S2). These features are shown in figure D.2(c) at high  $V_{max}$ , and figure D.2(e) at smaller  $V_{max}$ .

Quantitatively, we can compare simulation and experiment by observing that  $V_{max}$  grows in the experiment with the angle of inclination of the channel—that is, water flows

faster on steeper surfaces. Thus in figure D.2(d), we show a comparison between the maximum distance that particles travel up the channel as a function of angle of inclination of the channel (the relation between  $V_{max}$  and angle is derived in section D.5). Evidently, experiment and simulation show comparable increases in upstream contamination as the channel angle is decreased. Mechanistically, we note that upstream flow in both simulations and experiments appears where the downstream flow is slowest-at the back of the waterfall and along the sides of the channel.

Finally, we also tested the upstream contamination effect at both smaller and larger scales. At smaller scales, surface tension effects typically grow as scales diminish [99], so it can be anticipated that upstream contamination may increasingly be encountered in smaller scale applications [100]-e.g. cell culture [101] or free-surface microfluidics [102]. Indeed, it has long been known that bacteria actively manipulate surface tension gradients to control migration and swarming [103]. To assess upstream contamination in an archetypal bioengineering device, we pipetted deionized water into a Petri dish containing water on which fluorescein powder was sprinkled. In six out of 10 trials at pipette angles of  $20 \pm 5$  degrees to the horizontal, heights between 3 and 5mm, and flow rates of  $0.7 \pm 0.1 \text{mls}^{-1}$ , significant contamination inside the pipette was seen (shown in figure D.5 of section D.4 and video S3 of section D.2), and in seven out of 10 additional trials, contamination was seen either inside or outside of the pipette. Importantly, in both experiments and simulations, upstream contamination appears to rely on a differential in ambient fluid speed, and correspondingly, upstream flow was not encountered in our experiments if the pipette was held vertically. Nevertheless, we caution that we cannot rule out the possibility that upstream contamination could occur in uniform flows-especially at small scales.

At larger scales, we have performed two sets of tests. First, to study the effects of scale on flow up waterfalls, we repeated the experiments shown in figure D.1 using square channels of widths 3, 5 and 10cm. We confirmed that chalk powder continues to climb small waterfalls (heights less than 1cm) in all of these channels. Second, to study upstream flow in channels, we used a 4.5m long, 30cm wide, flume (described in [104]) filled with tap water, and found that contamination against a steady downstream flow

occurs over this scale as well. In figure D.3(a), we show a schematic of the flume. We found that inclining the chute bottom very slightly uphill produces a reproducibly steady and uniform flow, so that for all experiments described here, the flume was set at 1 degree uphill to the horizontal. For the experiments shown in figure D.3, this produced a water depth at the downstream end of the flume of 3cm and a depth at the upstream end of 5cm. In these experiments, we measured the downstream surface velocity to be  $3.6 \pm 0.1 \text{ cm s}^{-1}$  by timing how long individual small polystyrene beads dropped in the centre of the flow take to travel the length of the flume.

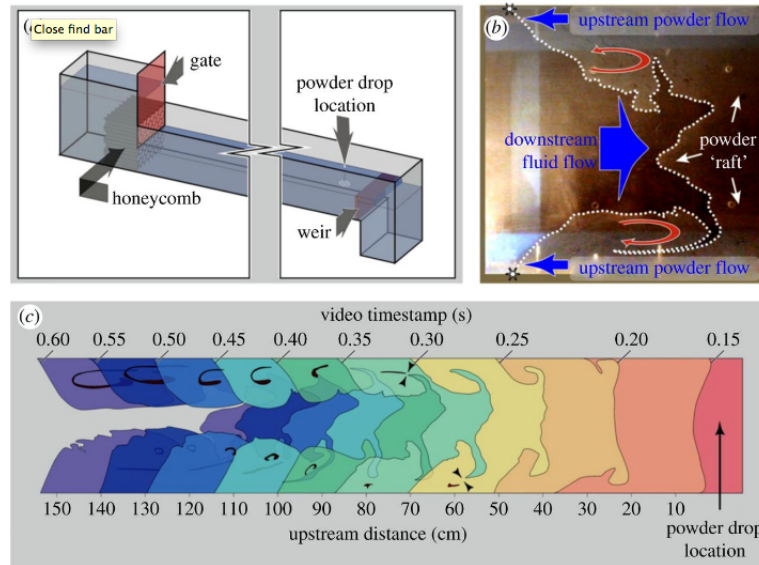


Figure D.3: Upstream contamination in 4.5m long, 30cm wide, flume. (a) Schematic of upstream and downstream portions of flume. Water is recirculated at a controlled rate (pump and plumbing not shown) from the downstream receiving tank to the upstream holding tank. Flow is laminarized using the honeycomb tubing indicated, and depth is controlled using the gate upstream and the weir downstream. Chalk powder is metered continuously near the downstream end, and powder flow is recorded with a video camera from above (see section D.2, video S4). (b) Snapshot taken about 30s into experiment, with competing downstream fluid flow at the centre of the flume and the upstream powder flow along channel sides identified in by straight arrows. This competition produces the powder raft shown and circulatory flow, indicated by curved arrows. Asterisks indicate the highest upstream points on the raft discussed in the text. (c) Leading edges of powder at 5s intervals during the first minute of the experiment. Edge locations are quantitatively approximate due to parallax and limited contrast, but are qualitatively veridical, as shown by the white dotted edge in (b). Circulatory regions identified in dark colouring contain no powder and are formed after pinch-off of elongated fingers at locations indicated by black arrowheads.

In this larger system, we metered chalk powder continuously from above at a fixed location near the downstream end of the flume (indicated in figure D.3(a,c)), and we recorded the powder flow from above with a video camera (see section D.2, video S4). We did not investigate climbing of a waterfall in the flume because this would have required a large quantity of powder that could foul the recirculation pump. Instead, we used the flume to focus on contamination in a larger scale channel as might occur upstream of a continuous waste discharge into a stream.

As in the smaller channel experiments shown in figure D.1, we find that upstream contamination is fastest along the edges of the channel and competes against downstream ambient flow in the centre of the channel to produce recirculation near the channel edges. Unlike the earlier experiments, the powder forms a contiguous raft that travels upstream across the width of the flume. The competing flows and the powder raft are indicated in figure D.3(b) in a snapshot taken 30s after the start of an experiment. Recirculation produces tendrils of entrained powder-free fluid as seen near the bottom of this figure.

The same can be seen in time-lapse images: in figure D.3(c), we show the leading edge of a raft as it travels upstream, traced from video images at 5s intervals. Tendrils in the raft appear here as well: these tendrils break off at times 0.30 and 0.35 (arrowheads in figure D.3(c)) to form recirculating powder-free islands that are highlighted in dark shading at later times. These islands continue to recirculate-and the raft continues to move upstream-as long as powder is metered downstream. When metering is halted, recirculation stops and the raft convects downstream into the holding tank.

Edges in figure D.3 are traced by hand. Gradient and Sobel edge-finding algorithms were also investigated, but were found to be ineffective due to the intrinsic low contrast of the powder-water interface, as well as being dominated by spurious edges caused by reflections and flume support members. A typical tracing is shown as a dotted line in figure D.3(b), and comparison with the video record can be made from section D.2, video S4.

We also varied the fluid flow speed by increasing the head in the upstream tank, with the goal of establishing the maximum speed,  $V_{max}$  that could be defeated by upstream contamination. However, we found that  $V_{max}$  depends on the rate of metering of powder,  $Q_{powder}$ : by increasing  $Q_{powder}$ , we could drive the raft of powder upstream at increasing downstream speeds-at least up to  $30\text{cm s}^{-1}$ , beyond which a prohibitive amount of powder was needed to sustain upstream contamination. Additionally, we investigated fixing  $Q_{powder}$ , but in that case, we found that as  $V_{max}$  was increased, the raft would approach a limiting upstream distance,  $D_{max}$  and stop, and as the flow speed was increased,  $D_{max}$  would decrease, and vice versa. Thus, for continuous deposition



of powder,  $V_{max}$  depends both on  $Q_{powder}$  and on  $D_{max}$ .

Therefore, to produce a unique measure of a threshold fluid speed that would out-compete upstream contamination, we metered a fixed quantity of powder (5.5g released over 3.5s) and evaluated the maximum speed,  $V_{max}$  at which the highest upstream points of the raft (asterisks in figure 3b) passed upstream of the deposit location. We found this criterion to be reproducible, yielding a maximum speed  $V_{max} \sim 24\text{cm s}^{-1}$  measured at the centre of the channel.

In conclusion, we have demonstrated that floating particles can travel upstream as much as 1cm up a waterfall and several metres up a channel against a downstream fluid flow. We have seen that this effect occurs for both pure ingredients (e.g. fluorescein in deionized water) and more common materials (e.g. tea in tap water). We have shown that upstream flow of contaminant particles can be generated by surface tension gradients that are established by the downstream flow of clean water into a contaminated reservoir, and we have seen upstream contamination in both small (millimetre scale) and large (metre scale) experiments.

## D.2 Supplementary Videos

- Video S1 - flow of floating chalk particles (white) up waterfall and inclined channel.  
<http://coewww.rutgers.edu/~shinbrot/temp/VideoS1.mov>
- Video S2 - simulated flow of floating point particles. <http://coewww.rutgers.edu/~shinbrot/temp/VideoS2.mov>
- Video S3- upstream contamination into pipette. <http://coewww.rutgers.edu/~shinbrot/temp/VideoS3.mov>
- Video S4 upstream contamination in flume. <http://coewww.rutgers.edu/~shinbrot/temp/VideoS4.mov>

### D.3 Tea Leaves flowing upstream into pot of initially clear water

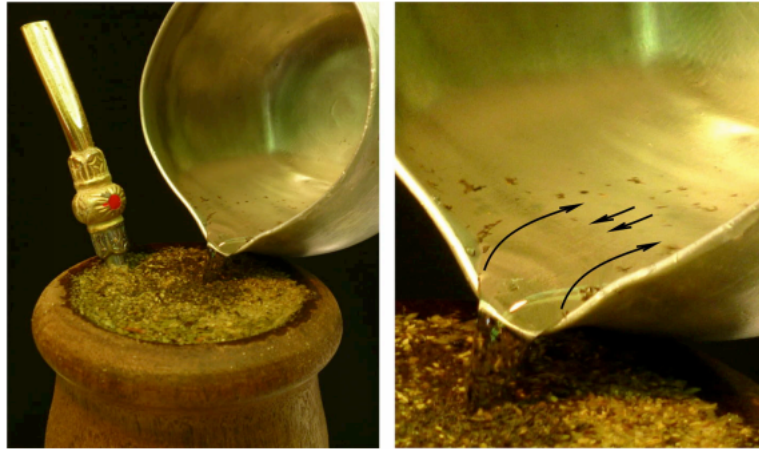


Figure D.4: Upstream contamination of Mate Tea.

Preparation of mate tea, showing tea leaves climbing up waterfall into pot of water. Enlargement to right shows tea leaves that have made their way from the cup into the pot, up a waterfall about 1 cm in height

#### D.4 Clear water being pipetted into reservoir of water containing fluorescent particles.

In multiple trials of the experiment shown in Fig. D.5, a plastic pipette was flushed with deionized water and dried with compressed air. The pipette was then filled with 11 ml of deionized water using a Thermo Scientific Matrix pipettor. 10 ml of this water was then discharged using the pipettor, with the pipette held between 2 and 5 mm above the water surface of a Petri dish, onto which powdered fluorescein had been sprinkled. The pipette was held at an angle measured to be  $20 \pm 5$  degrees, and was never permitted to become submerged into the receiving water. All trials were videotaped, and any trial in which the pipette tip was observed to become submerged was discarded from consideration. Angle and height measurements were obtained by analyzing video footage (cf. Video S3) with ImageJ software. The rate of discharge from the pipette was measured to be  $0.7 \pm 0.1 \text{ ml/s}$  in a separate evaluation. After each trial, the exterior of the pipette tip was wiped with a clean paper towel to remove surface liquid, and the pipette was exposed to UV light and photographed. 10 ml was then drained from the Petri dish using a separate pipette, and the procedure was repeated.

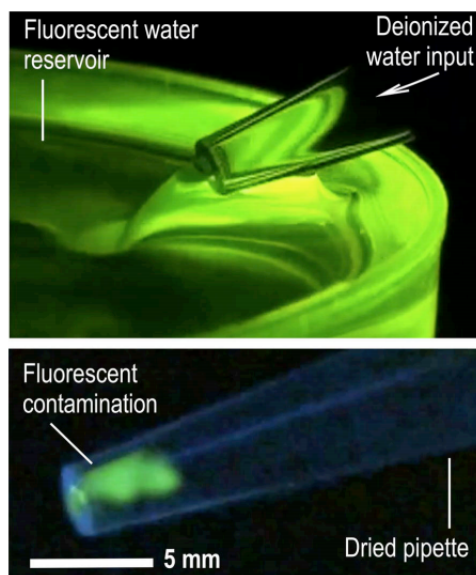


Figure D.5: Upstream Contamination in pipetted water

Pipetting of deionized water into Petri dish containing fluorescein illuminated with UV light. Pipette is initially washed in deionized water, dried with compressed air and confirmed to be free of fluorescence. Upper panel shows water stream during pipetting of with an electric pipettor. The discharge rate is measured to be  $0.7 \pm 0.1$  ml/sec, and the pipettor is initially filled with 11 ml, of which 10 ml was discharged. Lower panel shows pipette tip after pipetting tip has been wiped with clean towel to remove any external contamination, so the illuminated fluid is inside the pipette tip, indicating that it was not transferred by splashing or the “teapot effect” evident in the upper panel.

## D.5 Computational Simulations

As described in the text, a number of particles are tracked on a 2D domain and subjected to simulated elastic forces and an entraining fluid velocity. In detail, these two influences are defined as follows.

The elastic response of particles on the water surface is defined by specifying a Gaussian concentration field surrounding each particle. To find the concentration at the location,  $\vec{r}_i$ , of particular particle, I, due to a second particle, j, at another location,  $\vec{r}_j$ , we compute:

$$C_{ij} = A_g e^{\left(\frac{-r_{ij}^2}{\sigma_g^2}\right)} \quad (\text{D.1})$$

where the parameter values used in this paper are  $A_g = 9$  and  $\sigma_g = 1/\sqrt{150}$ . These values were chosen because they produce flows similar to those seen in experiments; tests using different values ranging over at least an order of magnitude for each parameter were also performed, yielding the following results. Moreover, tests using other decreasing functions, including  $1/r$  and  $\text{erfc}(r)$  produce qualitatively similar behaviors. As  $A_g$  is increased (decreased) particles effectively repel one another more strongly (weakly), and as  $\sigma_g$  is increased (decreased), the distance over which particles interact is increased (decreased). The qualitative flow (up the back of the waterfall and sides of the channel, down the center) is unchanged by these variations.

As described in the text, given a concentration  $C_{ij}$ , the elastic force in the direction on the i-th due to the j-th particle is assumed to be reduced proportionally to  $C_{ij}$ , and we take the proportionality constant to be unity. We make use of the fact that a reduction in attractive force on an elastic surface is indistinguishable from an increase in repulsive force: this permits us to simply treat pairs of particles on the surface as repelling with force,  $\vec{C}_{ij}$ , of magnitude  $C_{ij}$  and direction along the vector connecting the two particles. We assume superposition, again as mentioned in the text, so the vector sum of all forces acting on each particle produces a net force that we iterate forward by a timestep  $\Delta t = 0.1$  using simple Euler integration. Assuming that each particle has unit mass, we obtain:

$$\vec{r}_i(t + \Delta t) = \vec{r}_i(t) + \Delta t \cdot \vec{v}_i(t) + \frac{\Delta t^2}{2} \sum_{i \neq j} \vec{C}_{ij} \quad (\text{D.2})$$

$$\vec{v}_i(t + \Delta t) = \gamma \vec{v}_i(t) + \Delta t \sum_{i \neq j} \vec{C}_{ij} \quad (\text{D.3})$$

where  $\vec{r}_i(t)$  and  $\vec{v}_i(t)$  are respectively the position and velocity of the  $i$ -th particle at time  $t$ . The constant  $\gamma$  is included to account for viscous losses: for  $\gamma = 1$ , particles would be fully inertial; for  $\gamma = 0$ , particles would act in the Stokes regime with no inertia. We use  $\gamma = 1/2$  in the simulations shown; trials using smaller  $\gamma$  behave essentially identically, while for larger  $\gamma$  the simulations become increasingly computationally unstable, and smaller  $\Delta t$  values are required to produce smooth particle motions. The boundaries in the channel region (described next) are taken to be specular, so that particles that stray outside of the allowed domain,  $-L/2 < x < L/2$ , due to elasticity or noise (discussed shortly), are reflected back into the domain by reversing their velocity component normal to the channel boundary.

Every timestep, we evolve all particles forward using Eqn's. [D.2,D.3], after which we take them to be advected passively by the ambient fluid velocity. This we define as follows. In the channel region, we assume that particles follow a fluid flow downstream with a velocity that is defined by the Poiseuille relation,

$$\vec{V}_{channel} = V_{1max}[1 - (2x/L)^2]\hat{y} \quad (\text{D.4})$$

where  $V_{1max}$  and  $L$  are constants defining the centerline speed and the channel width,  $x$  is the spanwise coordinate, and  $y$  is the streamwise unit vector. The use of the laminar Poiseuille relation is justified by a calculation of the shallow water Reynolds number [98]

$$Re_{shallow} = \left(\frac{depth}{width}\right)^2 \frac{V \cdot L}{v} \quad (\text{D.5})$$

which is  $Re_{shallow} \sim 8$  for our system, using  $depth = 0.2cm$ ,  $width = 2cm$ ,  $V = 4cm/s$ ,  $L = 2cm$ , and  $v = 0.01P$ .

The channel flow feeds the waterfall, and in that region, boundary conditions are periodic in the x-direction: we take  $x = r \cdot \phi$ , where  $r$  is the radius of the waterfall, taken to be  $r \equiv 1/2\pi$ , and  $\phi$  is the azimuthal angle. Flow in the y-direction is not known in closed form, but flow toward the back of the waterfall is slowed by contact with the channel bottom, while flow toward the front is unconstrained, so as described in the text to lowest order the flow must depend on:

$$\vec{V}_{waterfall} = V_{2max} \left[ \frac{1 + \cos(2\pi x/C)}{2} \right] \hat{y} \quad (\text{D.6})$$

where  $C$  is the circumference of the waterfall which we take to be constant, and  $V_{2max}$  is defined to conserve mass, so that the velocities integrated over the widths in the channel and waterfall regions are identical: this defines  $V_{2max}$  in terms of  $C$ ,  $L$ , and  $V_{1max}$ . Conservation of mass at the surface is not strictly required, but is plausible and reduces the number of free parameters in the problem. The last thing to be prescribed is the circumference,  $C$ , which we observe from experiments to be close to  $L/2$  (cf. Fig. D.1(b)), so to close the problem, we take  $L=1$  and  $C = L/2$ , and for simplicity we define the boundaries to change smoothly, as shown in Fig. D.2(c), from the channel to the waterfall regions using the form,  $Width = [3 - \tanh(4y)]L/4$ . A last addition to the time evolution is that we include noise by adding random white noise with maximum amplitude  $\pm 0.01$  to both  $V_x$  and  $V_y$  once per timestep.

Finally, in order to correlate the dimensionless model (where fluid flow speed depends on  $V_{max}$  expressed in channel widths per 10 timesteps) with the dimensional experiment (where the fluid speed in centimeters/sec. is determined by the inclination angle,  $\theta$ , of the channel), we perform dimensional analysis guided by the Buckingham  $\pi$  theorem [105]. Surface tension is defined as force per unit length, so we consider a unit length,  $\lambda$ , of fluid at the center of the channel, with density  $\rho$  and viscosity  $v$  that is accelerated in the downstream direction by  $A_{down} = g \cdot \sin(\theta)$  where  $g$  is gravity. At steady state, this volume is slowed by an equal acceleration  $A_{up}$  that we assume grows with  $V_{max}$ . This problem consists of 5 parameters,  $\lambda$ ,  $\rho$ ,  $v$ ,  $A_{up}$ , and  $V_{max}$ , that are defined in terms of 3 physical quantities, mass,  $M$ , length,  $L$  and time,  $T$ , so Buckingham  $\pi$  tells us that the problem must depend on  $5 - 3 = 2$  dimensionless groups. If  $Re_{shallow}$



is one group, a second is  $C_d = A_{up} \cdot \lambda / V_{max}^2 = g \cdot \lambda \cdot \sin(\theta) / V_{max}^2$ , so that:

$$V_{max} \propto \sqrt{g \cdot \lambda \cdot \sin(\theta)}. \quad (\text{D.7})$$

Thus in Fig. D.2(d), we plot on the abscissa the inclination angle,  $\theta$ , for experimental data, alongside  $\theta = \sin^{-1}(c \cdot V_{max}^2)$  for the simulation data, where  $c$  is a dimensional fitting constant taken to be  $c = 5$ . As for the ordinate axis, that is expressed in centimeters in the experiment, but is again dimensionless in the simulation, and so the ordinate in the simulation is scaled by a second dimensional fitting constant.